Manufacturing of Graphene Nanodisks for Surface Plasmon Measurements

Niko-Ville Hakkola

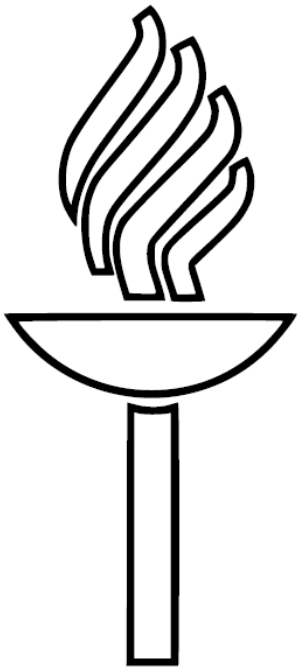

Master's Thesis
University of Jyväskylä
Department of Physics
27.11.2017
Supervisor-in-charge: Jussi Toppari
Supervisor: Tommi Isoniemi

Preface

The experimental and theoretical work for this Master's thesis has been conducted during June 2014 and November 2017 at the Nanoscience Center of the Department of Physics of the University of Jyväskylä.

I would like to thank Jussi Toppari for providing this interesting topic for my thesis and the opportunity to work in his research group and the valuable help provided. In addition, I would like to thank Tommi Isoniemi for his guidance all throughout the experimental work. Also I would like to thank all of the personnel around the Nanoscience Center in Jyväskylä who have helped me in any way during this process and my friends and family for their continuous support.

Jyväskylä, November 2017

Niko-Ville Hakkola

Abstract

Graphene has emerged as a promising candidate to replace noble metals as a plasmonic material due to its unique properties and tunability. Graphene plasmonics offer possibilities of controlling light in nanoscale devices and merging optics with electronics. The goal of this thesis was to modify a hole-mask colloidal lithography method to find out a fabrication method that could be used to manufacture samples of a randomly organized array of 200 nm sized graphene nanodisks with some distance between them and with a good amount of the sample covered by the nanodisks. These graphene nanodisks would then be studied for their surface plasmon properties by measuring their infrared spectra with a Fourier-transform infrared (FTIR) spectroscope. The energies and strengths of these surface plasmons in graphene nanodisks can be tuned by electrical doping which was studied as well.

The manufacturing of graphene nanodisks was rather successful. A fairly reliable method to produce nanodisks was successfully developed with arrangement and amount of nanodisks just as desired but with some impurities still left in the samples, probably due to the final removal and cleaning with acetone. However, the surface plasmon measurements were a failure and no plasmons could be seen in any of the samples which could be due to multiple reasons such as the graphene not being good enough for measurements or the spectroscope not being able to reliably measure these extremely thin samples. The measurements could have been improved by an even better coverage of the graphene nanodisks in the samples.

Tiivistelmä

Grafeeni on ilmestynyt tieteen rintamalle kovalla ryminällä vasta viimeisen 13 vuoden aikana, mutta on jo nyt yksi mielenkiintoisimmista tutkimuskohteista, jolla voisi olla lukuisia sovelluksia tulevaisuudessa. Grafeeni on ilmestynyt myös plasmoniikan tutkimuskohteeksi sen lukuisten ainutlaatuisten sähköisten ja optisten ominaisuuksien takia ja sen ominaisuuksien muokattavuuden helppouden takia. Grafeeni voisi mahdollisesti korvata yleisesti käytössä olleet jalot metallit kuten kullan ja hopean pintaplasmonien tuotossa ja tutkimuksessa ja voisi johtaa uudenlaiseen valon kontrollointiin nanoskaalassa ja optiikan ja elektroniikan yhdistämiseen tässä pienessä mittakaavassa.

Tässä työssä tavoitteena oli ”hole-mask colloidal”-litografiamenetelmän muokkaaminen ja tarvittavien valmistusvaiheiden tutkiminen ja kehitys. Tavoitteena oli saada tehtyä näytteitä, joilla olisi 200 nm kokoisia grafeeninanokiekkoja sopivalla etäisyydellä toisistaan ja jotka kattaisivat suurimman osan näytteen pinnasta. Näitä grafeeninanokiekkoja tutkittaisiin sitten infrapunaspektroskopialla. Tavoitteena olisi saada näkyviin pintaplasmoneista johtuvia resonansseja spektreissä sekä näiden voimakkuuden ja aallonpituuden muuttaminen sähköisellä seostamisella eli tässä tapauksessa tuomalla eri vahvuista hilajännitettä grafeenikiekoille.

Grafeeninanokiekkojen valmistus onnistui kohtuullisen hyvin ja varsin luotettava valmistusmenetelmä saatiin kehitettyä, vaikkakin jonkinlaista epäpuhtautta näytteisiin jäikin todennäköisesti asetonipuhdistuksesta johtuen. Pintaplasmonimittaukset eivät sen sijaan onnistuneet lainkaan eikä plasmoniresonansseja saatu näkyviin missään näytteissä. Tälle voisi useitakin syitä löytyä, mutta mahdollisesti käytetty grafeeni ei ollut kovin hyvää näitä mittauksia ajatellen tai käytetty spektrometri ei ollut tarpeeksi hyvä näin ohuiden näytteiden mittaamiseen. Mittauksia olisi voitu myös parantaa, jos näytteiden pinta-alasta suurempi osa olisi sisältänyt grafeeninanokiekkoja.

Contents

1 Introduction

Richard Feynman introduced the idea of controlling and manipulating individual atoms and molecules in his famous speech in 1959. It took until the 1970s before nanotechnology as a term was used and the 1980s before it became widely known and started growing with the invention of the scanning tunneling microscope. Since then nanotechnology has been one of the most rapidly growing fields of research with ties to all the other science fields and with countless of applications already in use and countless of others being developed.

Surface plasmons are collective electron oscillations that exist at the interface between two materials. Usually between a dielectric material such as air or vacuum and a metal but any two materials where the real part of the dielectric function changes sign across the interface can result in surface plasmons. Surface plasmons propagate along the interface in wave-like formations decaying with respect to travel distance and the properties of the materials. By changing the materials and their structures and properties at the nanoscale, surface plasmons properties can be changed as well as tailored for specific applications and for different subwavelength optics which is why surface plasmons are being studied by scientists from many different fields.

Interest in the field of plasmonics has increased significantly in the past few decades, especially the study of surface plasmons. The advancements in nanotechnology and optics and the merging of these fields has led to remarkable insights into the nanoscale interactions of light and matter. The history of plasmons can be dated perhaps as far back as 1902 when Robert Williams Wood reported, albeit without a plausible explanation, results of uneven distribution of visible light in a diffraction grating spectrum which can be related to a plasmon phenomenon [1]. Some progress was made in the following decades by Ugo Fano [2] and by David Pines [3] but Rufus Ritchie in 1957 was the first to show theoretical descriptions of surface plasmons via the diffraction of electron beams at thin metal films and summarised the studies during the past years into a general theory [4]. Ritchie et al. in 1968 also linked his general theory with the original work done decades ago on diffraction gratings in the optical spectrum [5]. Another important advance in studying surface plasmons was made by Andreas Otto, Erich Kretschmann and Heinz Raether in 1968 [6–8] when they presented practical methods on how to

conduct optical excitations of surface plasmons on metal films. These experiments made researching surface plasmons much more easily accessible to other scientists, thus rapidly increasing the interest and progress in this field.

Some interesting applications of surface plasmons could include miniaturized and much smaller photonic circuits than currently achieved [9,10], high-density optical data storage [11] and enhancement of absorption of light in solar cells [12]. Surface plasmons are already widely used in different sensors, e.g., biosensors [13] and will be used even more in the future.

Graphene is a two-dimensional allotrope of carbon. It is a monolayer of hexagonally structured carbon atoms in a honeycomb lattice. Graphene has emerged into the fields of science as a new and remarkable material only very recently but has already been researched immensely in the last decade. Graphene has also emerged as a possible replacement for the traditional noble metals in producing surface plasmons due to its unique properties and great tunability. Graphite as a material has been used throughout the history extensively but the first observation of graphene was made in 1859 by Benjamin Brodie when he exposed graphite to strong acid [14] unknowingly producing a suspension of tiny crystals of graphene oxide, a graphene sheet densely covered with hydroxyl and epoxide groups. This graphene-oxide suspension was studied in 1948 by G. Rüss and F. Vogt with a transmission electron microscope observing flakes with thickness of a few nanometres [15], and continuing that in 1962 Ulrich Hofmann and Hanns-Peter Boehm identified monolayers of graphene [16]. The first theoretical studies and descriptions of graphene were made by Phil Wallace in 1947 trying to understand graphite's electronic properties and calculating band structures [17]. It took until 2004 before graphene was truly discovered, isolated and characterized by Andre Geim and Konstantin Novoselov in their famous study where they used a simple but effective mechanical exfoliation method by separating monolayers of graphene from graphite using tape and transferring those monolayers into silicon substrates [18].

The unique properties of graphene have made it a fascinating research subject with a bright future. Interest in graphene has also led to the discovery of other monolayer materials with similar properties. Producing was at the start incredibly expensive but with the enormous interest that graphene has attracted, new producing techniques have been invented

making it more affordable, thus making potential applications sensible and within reach. Graphene could be utilized in various ways in electronics and graphene photonics and optoelectronics. Possible applications could include transparent electrodes, for example for solar cells and LCD displays [19–21], flexible electronic devices [22] and graphene photodetectors improved by plasmonic nanostructures [23] to give few examples, but the possibilities seem to be endless.

The motivation behind this thesis was the recent progress made with surface plasmons, graphene and surface plasmons in graphene. Graphene with its unique electrical and optical properties has emerged as an interesting material for producing surface plasmons and by combining these relatively new and vibrant fields of research together could provide intriguing applications. Surface plasmons and graphene were studied here by utilizing various nanofabrication methods. Tunability of plasmons was studied in nanostructured graphene as demonstrated by Fang et al. [24] and graphene was nanostructured by using a modified hole-mask colloidal lithography method [25].

2 Theory

2.1 Surface Plasmons

In this chapter the theory behind surface plasmons is discussed in detail. Surface plasmons most often couple with photons, visible light, to form surface plasmon polaritons (SPPs). SPPs are of the most interest in terms of research and possible applications. The dispersion relation, the propagation distance, and the excitation of surface plasmon polaritons will be discussed among other things.

2.1.1 Surface Plasmon Polaritons

Surface plasmon polaritons are formed at the surface of a metal and a dielectric material from the quantized excitations of electrons and photons coupling together. The free electrons at the surface of a metal interact with the incoming photons becoming excited and collectively oscillating in resonance with the photons. This resonant interaction is the basis behind surface plasmon polaritons, resulting in wave-like formations that propagate along the interface between the materials. These waves decay with respect to travel distance and the properties of the materials, and are confined to the vicinity of the interface of the materials. The field amplitudes of surface plasmon polaritons exponentially decay into both materials away from the interface. The dampening occurs mostly by absorption in the metal and by scattering. Due to high losses the SPPs propagate most efficiently in the visible and near-infrared region. Surface plasmon polaritons are sensitive to surface conditions, i.e., the properties of the materials, surface structure, and defects on the surface. This sensitivity stems from the strong confinement of the surface plasmon polaritons which leads to an enhanced electromagnetic field at the interface resulting in their sensitivity. [26] A simple illustration of a surface plasmon polariton is shown in figure 2.1.

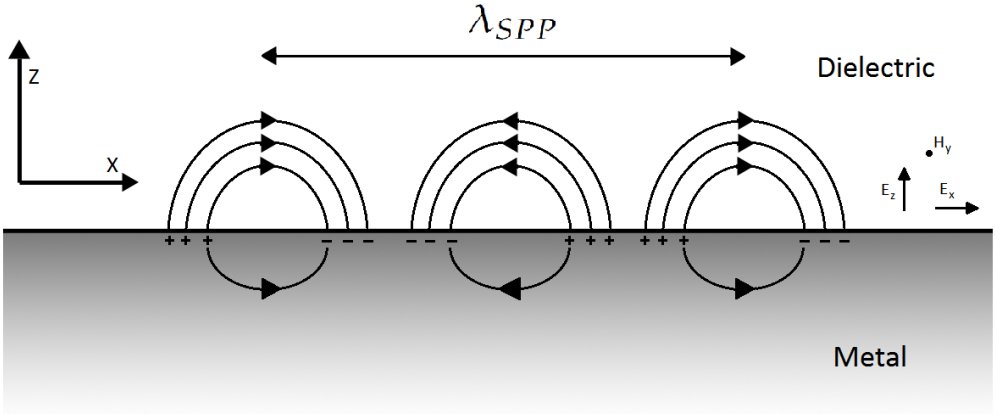

Figure 2.1: An illustration of a surface plasmon polariton at a planar interface between a metal and a dielectric material.

2.1.2 Dispersion Relation

The physical properties and the behavior of surface plasmon polaritons can be investigated by considering the simplest geometry between materials as shown in figure 2.1, a single planar interface between a dielectric material and a metal along which the SPP will be propagating. The solutions for this system can be obtained by solving the Maxwell equations. The equations in this chapter are mostly based on [27]. The Maxwell equations for this system, assuming that the external (free) charge density $\rho = 0$, are

$$\begin{cases} \nabla \times H_i = \dfrac{\partial D_i}{\partial t}, \\ \nabla \times E_i = -\dfrac{\partial B_i}{\partial t}, \end{cases} \tag{2.1.1}$$

$$\begin{cases} \nabla D_i = \epsilon_0 \nabla (\epsilon_i E_i) = 0, \\ \nabla B_i = \mu_0 \nabla \mu_i H_i = 0, \end{cases} \tag{2.1.2}$$

where H, E, D and B are respectively the magnetic field, the electric field, the dielectric displacement and the magnetic induction or magnetic flux density. ϵ_0 and μ_0 are the electric permittivity and the magnetic permeability of vacuum, respectively. The subscript i will later refer to either the metal or the dielectric material with $i = m$ and $i = d$.

Electromagnetic (EM) waves are composed of electric and magnetic fields. EM waves can be polarized and are often times categorized into trans-

verse electric (TE), also called s polarized or transverse magnetic (TM), also called p polarized. EM waves can however be combinations of these both or even elliptically polarized. The solutions for the Maxwell can be also divided into TE and TM polarized waves. In TE the electric field is parallel to the interface while in TM the magnetic field is parallel to the interface. The electric field propagates in the (x,z) plane and the magnetic field in the (x,y) or (y,z) plane. For the dielectric medium where $z > 0$ the following equations can be obtained

$$\begin{cases} E_d = (E_{xd},0,E_{zd})\mathrm{e}^{\mathrm{i}(k_{xd}x+k_{zd}z-\omega t)}, \\ H_d = (0,H_{yd},0)\mathrm{e}^{\mathrm{i}(k_{xd}x+k_{zd}z-\omega t)}, \end{cases} \tag{2.1.3a}$$

where ω is the frequency of light and $k_d = (k_{xd},0,k_{zd})$ is the wavenumber in the dielectric medium. Similarly for the metal where $z < 0$ the following equations can be obtained

$$\begin{cases} E_m = (E_{xm},0,E_{zm})\mathrm{e}^{\mathrm{i}(k_{xm}x+k_{zm}z-\omega t)}, \\ H_m = (0,H_{ym},0)\mathrm{e}^{\mathrm{i}(k_{xm}x+k_{zm}z-\omega t)}. \end{cases} \tag{2.1.3b}$$

For the equations (2.1.3) to properly describe the exponential dampening of the electric and magnetic fields from the interface of the material, k_{zi} must be imaginary. Continuity of the electromagnetic field and its components leads to relations $E_{xd} = E_{xm}, H_{yd} = H_{ym}$. By inserting these relations into equations (2.1.3) another relation can be obtained for the x component of the metal and the dielectric wavenumbers $k_{xd} = k_{xm} = k_{SPP}$. k_{SPP} is now the surface plasmon polariton wavenumber. Combining then equations (2.1.3) and the Maxwell equations (2.1.2) results in

$$k_{zd}H_{yd} + \frac{\omega}{c}\epsilon_d E_{xd} = 0, \tag{2.1.4a}$$

$$k_{zm}H_{ym} - \frac{\omega}{c}\epsilon_m E_{xm} = 0, \tag{2.1.4b}$$

where $c = \frac{1}{\sqrt{\epsilon_0\mu_0}}$ is the speed of light in vacuum. Combining these equations (2.1.4) with the previously mentioned relations $E_{xd} = E_{xm}, H_{yd} = H_{ym}$ leads to

$$\frac{k_{zd}}{\epsilon_d} + \frac{k_{zm}}{\epsilon_m} = 0. \tag{2.1.5}$$

The continuity condition for the in-plane wavenumber results in the total wavenumber in medium i being

$$k_i^2 = k_{SPP}^2 + k_{zi}^2 = \epsilon_i \left(\frac{\omega}{c}\right)^2. \tag{2.1.6}$$

This can be then rearranged into an explicit expression for the surface plasmon polariton wavenumber k_{SPP} thus arriving at the dispersion relation for the surface plasmon polaritons

$$k_{SPP} = \frac{\omega}{c}\sqrt{\frac{\epsilon_d \epsilon_m}{\epsilon_d + \epsilon_m}}. \tag{2.1.7}$$

The dispersion relation of surface plasmon polaritons expresses the relation between the angular frequency ω and the wavenumber k_{SPP} of the surface plasmon polaritons. A wavenumber is the magnitude of a wavevector which can be used to describe waves pointing in the direction of their phase velocities. The SPP dispersion relation depends on the relative permettivities (dielectric functions) ϵ_m and ϵ_d of the metal and the dielectric. The permittivity of a material tells the encountered resistance when an electric field is being formed in the material. In dielectric materials the permittivity is usually only weakly dispersive so in terms of SPPs the permittivity of the metal is more intriguing.

SPPs involve charges at the surface of the metal. These charges can exist if the electric field component E_z changes sign across the interface. The displacement field component D_z in the same direction must be conserved. The displacement field and the electric field have a relation of $D_z = \epsilon E_z$. This means that the permittivities of the media must have opposite signs to sustain SPPs. The same conclusion can be made from equation (2.1.5). The permittivities of dielectric materials are positive so the permittivity of the metal must be negative. There are numerous metals for which ϵ_m has a rather large negative real part such as noble metals gold and silver. This is why the permittivity of the metal is more intriguing when studying SPPs.

The relative permittivities of metals can be studied by looking at the Drude-Sommerfeld theory and the dielectric function given by the theory [26]

$$\epsilon_m(\omega) = 1 - \frac{\omega_p^2}{\omega^2 - \mathrm{i}\Gamma\omega}, \tag{2.1.8}$$

where ω_p is the plasma frequency and Γ is the scattering rate used to account for dissipation of the electron motion. A dispersion relation can be plotted and is shown in figure 2.2. Only the real part of $\epsilon_m(\omega)$ is considered and ϵ_d (e.g. $\epsilon_{air} = 1$) is assumed to be real, positive and independent of ω. The dispersion relation of light in the dielectric medium is also plotted and is called the light line $\omega = ck_x$. Also plotted is the tilted

light line $\omega = ck_x/n$ which will be discussed later. From the SPP dispersion relation it can be seen that the SPP always gets larger values than the light line and also cannot get larger values than the surface plasmon frequency $\omega_{sp} = \frac{\omega_p}{\sqrt{1+\epsilon_d}}$. [28], [29, p. 387-390]

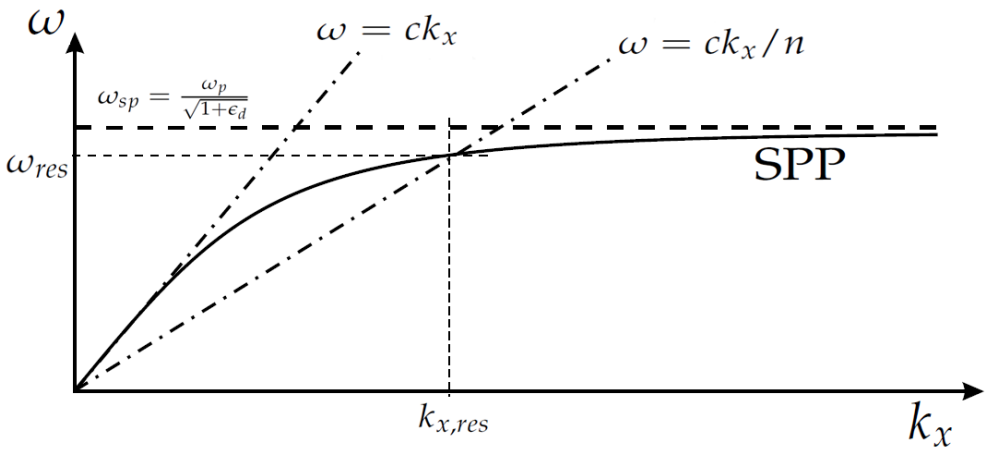

Figure 2.2: Surface plasmon polariton dispersion relation at a dielectric-metal interface. Visible in the picture are the light line $\omega = ck_x$, a tilted light line $\omega = ck_x/n$, the surface plasmon frequency $\omega_{sp} = \frac{\omega_p}{\sqrt{1+\epsilon_d}}$ and the resonant point where the tilted light line crosses the SPP. [29, p. 389]

2.1.3 Wavelength and Propagation Distance

Considering the complex nature of the metal's dielectric function the wavelength of the SPPs can be obtained. The equations in this chapter are mostly based on [26]. The relative permittivity of the metal can be written as

$$\epsilon_m = \epsilon'_m + \mathrm{i}\epsilon''_m, \tag{2.1.9}$$

which now contains the real and imaginary parts of the dielectric function. Under the assumption that $|\epsilon''_m| \ll |\epsilon'_m|$ the complex SPP wavenumber also containing the real and imaginary parts can then be written as

$$k_{SPP} = k'_{SPP} + \mathrm{i}k''_{SPP}. \tag{2.1.10}$$

The real and imaginary parts of the wavenumber are

$$k'_{SPP} = \frac{\omega}{c}\sqrt{\frac{\epsilon_d \epsilon'_m}{\epsilon_d + \epsilon'_m}}, \tag{2.1.11a}$$

$$k''_{SPP} = \frac{\omega}{c}\frac{\epsilon''_m}{2(\epsilon'_m)^2}\left(\frac{\epsilon_d \epsilon'_m}{\epsilon_d + \epsilon'_m}\right)^{\frac{3}{2}}. \tag{2.1.11b}$$

The SPP wavelength λ_{SPP} is defined as $\lambda_{SPP} = \frac{2\pi}{k'_{SPP}}$ therefore arriving at

$$\lambda_{SPP} = \lambda_0\sqrt{\frac{\epsilon_d + \epsilon'_m}{\epsilon_d \epsilon'_m}}, \tag{2.1.12}$$

where $\lambda_0 = \frac{2\pi c}{\omega}$ is the wavelength of light used to excite SPPs. This is because the excitation light wavenumber in free space is $k_0 = \frac{2\pi}{\lambda_0}$ and the dispersion relationship with frequency is $k_0 = \frac{\omega}{c}$.

Relation (2.1.12) of the SPP wavelength demonstrates that in the visible and near-infrared regions the SPP wavelength λ_{SPP} will always be slightly less than the excitation light wavelength λ_0. So the ratio $\frac{\lambda_{SPP}}{\lambda_0}$ will always be less than 1 and is dependent on the permittivities of the metal, the dielectric, and the excitation wavelength. For example at the interface of air/silver the values will be between $0.9 - 0.99$ in the $400 - 1600\,\text{nm}$ spectral range. [26] This ratio also reflects the bound nature of SPPs at the interface. It is also an extremely important starting point for the whole field of subwavelength optics and also shows how length scales of structures need to be of the order of wavelength involved to be able to be used to control and manipulate SPPs. The propagation distance of SPPs has to also be at least the length of a few times their wavelength so that they can be manipulated by the surface structures.

The propagation distance of surface plasmon polaritons δ_{SPP} can be calculated from the imaginary part of the SPP wavenumber (2.1.11b) by $\delta_{SPP} = \frac{1}{k''_{SPP}}$ and is therefore

$$\delta_{SPP} = \lambda_0\frac{(\epsilon'_m)^2}{2\pi\epsilon''_m}\left(\frac{\epsilon_d + \epsilon'_m}{\epsilon_d \epsilon'_m}\right)^{\frac{3}{2}}. \tag{2.1.13}$$

This tells the distance over which the electric field of the SPP falls to $1/e$ of its initial value due to ohmic losses in the metal. The propagation distance for silver in the visible and near-infrared range of $400 - 1600\,\text{nm}$

is approximately $20 - 340\,\mu m$ with the propagation distance increasing in respect of the wavelength [26]. Distances of even centimeters can be achieved for the propagation distance with processes utilizing symmetrically clad thin metal films where two SPP modes could be coupled together [30]. The SPP propagation distance is significantly longer than the SPP wavelength (as seen in figure 2.3) meaning that they can be manipulated by surface structures such as gratings and other periodic structures where SPPs can interact over many periods as speculated above. Determining and examining the SPP propagation distances is important for the consideration of photonic circuits because they represent an upper limit on the size of the structures that could be manufactured to utilize SPPs in various applications.

The penetration depth of surface plasmon polaritons can be obtained by considering the wavenumbers of the SPP and light. Light with free space wavevector k_0 in a material has a total wavevector of $\epsilon_i k_0^2$. Penetration of the fields occurs perpendicular to the propagation direction, i.e., in the z-direction. A previously mentioned relation (2.1.6) between the total wavevector and the z-component of the wavevector is needed. The SPP wavevector is always greater than the wavevector of light freely propagating so $k_{SPP}^2 > \epsilon_i k_0^2$ meaning that in both materials the z-component of the wavevector is imaginary and represents the attenuation of the fields with respect of distance into the materials. The penetration depths into the dielectric δ_d and the metal δ_m can then be calculated by combining the SPP dispersion relation (2.1.7) with the relation (2.1.6)

$$\delta_d = \frac{1}{k_0} \left| \frac{\epsilon_m' + \epsilon_d}{\epsilon_d^2} \right|^{\frac{1}{2}}, \tag{2.1.14a}$$

$$\delta_m = \frac{1}{k_0} \left| \frac{\epsilon_m' + \epsilon_d}{\epsilon_m'^2} \right|^{\frac{1}{2}}. \tag{2.1.14b}$$

Again for silver the penetration depths in the visible and near-infrared region ranges for the dielectric from a few hundred nm to a few µm increasing with the wavelength. For the metal the penetration depth is much smaller, only around $25 - 30\,nm$ and decreases with the wavelength. [26]

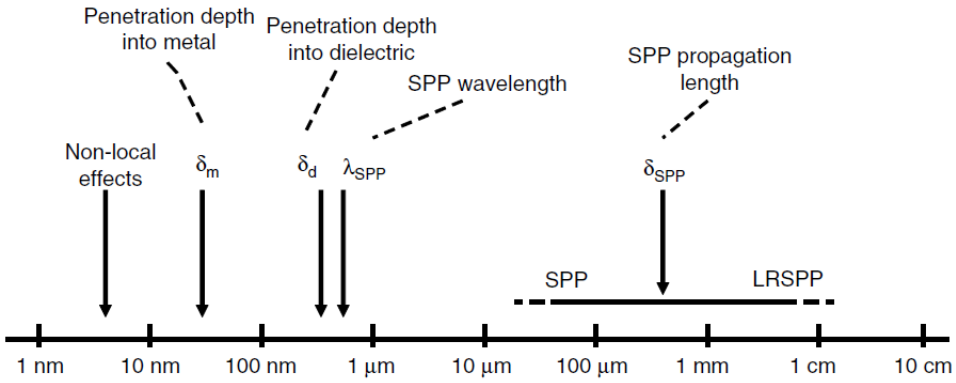

Figure 2.3: Surface plasmon polariton length scales in the visible and near-infrared range on a logarithmic scale. [26]

2.1.4 Excitation of Surface Plasmon Polaritons

The most important thing to consider when trying to excite surface plasmons with light is that the momentums $\hbar k$ of the plasmon and the photon have to match at the same energy for SPPs to be able to be excited. The wavevector k_x of SPPs is always greater than the wavevector k_0 of light in free space therefore light alone propagating in free space cannot excite plasmons at a planar interface. This is evident from the plotted dispersion relation in figure 2.2. The SPP dispersion curve always stays below the dispersion curve of light, the light line. The reason why SPPs have a greater momentum is the strong coupling between light and surface charges. [29, p. 387-390]

The momentum mismatch can be corrected with various methods. The simplest and most used method is to use evanescent waves created at the interface between a medium with a refractive index $n > 1$ such as glass to strengthen the light momentum. This way the light line is tilted by a factor of n as seen in figure 2.2. The tilted light line crosses the SPP dispersion curve at a resonant point where now at the same energy the momentums of the plasmon and the photon match and the SPP can be excited. Usually this is done with the help of prisms and either the Kretschmann [7, 8] or the Otto [6] configurations seen in figure 2.4. [29, p. 390-391]

In the Kretschmann configuration the light is guided through a prism before hitting the metal which is in contact with the prism. The angle of

incidence θ of the totally reflected beam inside the prism can be tuned to fulfill the condition of matching wavevector components because the wavevector of light is increased in the optically more dense medium. At this resonant angle where the condition is met light tunnels through the metal film and couples to SPPs at the metal-air interface. The situation can be described with [28]

$$k_{SPP} = \frac{\omega}{c}\sqrt{\epsilon_p}\sin\theta, \tag{2.1.15}$$

where ϵ_p is the relative permittivity of the prism.

The Otto configuration differs from the Kretschmann configuration in that there is a tiny air gap between the prism and the metal. This method is not as convenient because the control of the air gap is challenging but can be used for thicker metal films. The operating principle is the same and the same resonant condition (2.1.15) applies.

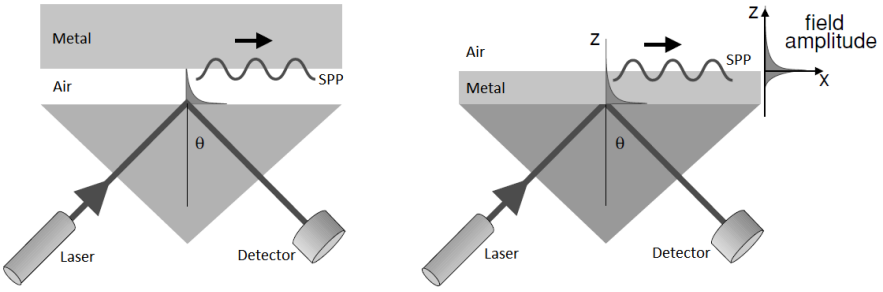

Figure 2.4: Left: Otto configuration. Right: Kretschmann configuration. [29, p. 389]

Another way to correct the momentum mismatch is to use grating couplers and the diffraction effects produced by them. The metal surface can be patterned with a grating of grooves or holes with the right peridiocity a over an extended region. The light diffracts from the grating in different ways and some components of that diffracted light can have wavevectors that coincide with the SPP wavevector and can therefore couple to SPPs. The situation can be described with [29, p. 392]

$$k_{SPP} = k_x = \frac{\omega}{c}\sin\theta \pm v\frac{2\pi}{a}, \tag{2.1.16}$$

where v is the order (1, 2, 3...) and $\frac{2\pi}{a}$ is the reciprocal vector of the grating. [31]

Diffraction can also occur from other surface features. Even from surface impurities and defects but in that kind of a randomly rough surface it is difficult to predict SPPs. In these surfaces there are diffracted light components to every direction and therefore the efficiency with which the light couples to SPPs is also quite low. Scattering of SPPs like this is still one of the most important things when considering the applications of SPPs. Studying surface features with the help of scattering of SPPs is key for determining optical properties of rough and nanostructured materials. The scattering of SPPs from features on the surface can be divided into three major categories. SPP reflection, i.e., the SPP scatters from a defect into another propagation direction, SPP transmission, i.e., the SPP propagates through the defect towards the initial propagation direction, and scattering of SPP into light. [28]

Another important thing to consider are the localized surface plasmons (LSPs). Considering other geometries than just planar dielectric-metal interfaces such as metallic particles or holes with different topologies, the oscillation of free electrons can be bound locally to these nanostructures or particles. These localized surface plasmons are a different type of excitations compared to the SPPs mentioned in the previous sections. LSPs can be directly excited by light with the correct frequency and polarization even if the wavevector of the exciting light doesn't match. LSPs therefore also decay with the emission of light. Their characterization depends on the structure's dimensions and dielectric function to which they are confined in and can be described using complex frequencies. They are visible as optical absorption without dispersion because of their nature. This is called the localized surface plasmon resonance (LSPR) and is widely used for applications of SPPs, e.g., various kinds of sensors. LSPs can have an important role in the behavior of SPPs on rough surfaces. LSPs can decay into SPPs and can be excited by the SPPs if their frequencies are close enough to each other thus enhancing the scattering of SPPs from defects on the surface. [28]

2.2 Graphene

Graphene with its unique properties has emerged as an interesting material to be researched in the recent years. The structure and properties of graphene will be discussed in this chapter to explain the reasons behind graphene's uniqueness.

2.2.1 Structure

Graphene is a two-dimensional material, a single layer of graphite made up of carbon atoms with sp^2 hybridization. The carbon atoms are organized in a hexagonal lattice resembling a honeycomb structure. This single layer of carbon atoms acts as the basis of many other allotropes of carbon such as 3D graphite, 1D nanotubes and 0D fullerenes.

A carbon atom has always four bonds. With the orbitals s, p_x and p_y the carbon atom forms covalent σ-bonds between the three neighbouring carbon atoms which are separated by a distance of $a = 1.42\,\text{Å}$ [32]. The remaining p_z orbital forms a π-bond perpendicular to the surface. These π-bonds from every carbon atom hybridize together to form the delocalized π- and π^*-bands.

The hexagonal lattice structure of graphene can also considered to be two interleaving triangular sublattices as seen in figure 2.5 where the different carbon atoms are denoted as either A or B and it is clearly visible in the picture how the sites of one sublattice are at the centers of triangles defined by the other sublattice. Stacking graphene layers together to form graphite happens due to weak van der Waals forces keeping the layers together, at a distance of $c = 3.354\,\text{Å}$ [33]. Stacking graphene layers can be done with either hexagonal AA stacking where the same atoms are at the same positions within sheets, Bernal ABAB stacking where the first and third layer are at the same position but the layer between has shifted or the rarer case of rhombohedral ABCABC stacking where the third layer shifts even further. A question arises as to how many layers of graphene there needs to be for it to be considered 3D graphite and distuingishing this is important. Therefore graphene can nowadays be separated into three different categories. Single layer graphene is just one sheet of carbon atoms. Bilayer graphene has two sheets together but still expressing similar properties. Few layer graphene has 3 to <10 sheets but is starting to lose some of the graphene's unique properties. From 10 layers upwards graphene is considered to be a thin film of graphite [34].

The lattice vectors as seen in figure 2.5 are [32]

$$a_1 = \frac{a}{2}(3,\sqrt{3}), \quad a_2 = \frac{a}{2}(3,-\sqrt{3}), \tag{2.2.1}$$

where a is the previously mentioned distance between carbon atoms. The

reciprocal lattice vectors are

$$b_1 = \frac{2\pi}{3a}(1,\sqrt{3}), \quad b_2 = \frac{2\pi}{3a}(1,-\sqrt{3}). \tag{2.2.2}$$

The three nearest-neighbour vectors can be written as

$$\delta_1 = \frac{a}{2}(1,\sqrt{3}), \quad \delta_2 = \frac{a}{2}(1,-\sqrt{3}), \quad \delta_3 = -a(1,0). \tag{2.2.3}$$

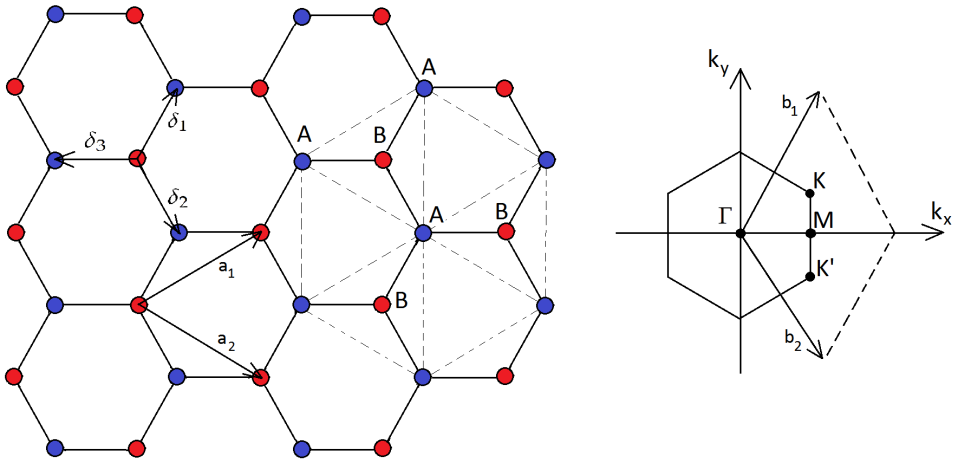

Figure 2.5: Left: Lattice structure of graphene with a_1 and a_2 being the lattice unit vectors and δ_i being the nearest-neighbour vectors. Right: First Brillouin zone (BZ) of the lattice structure with b_1 and b_2 being the reciprocal lattice vectors, Γ center of the BZ, M center of an edge, K and K' the Dirac points, and k_x and k_y the electron momentums in x- and x-directions. [32]

The strong in-plane σ-bonds which form the sp^2 hybridized lattice of graphene are responsible for graphene's incredible mechanical properties. Graphene is one of the strongest materials in the world. Intrinsic tensile strength for graphene has been found to be $\sigma_{int} = 130\,\text{GPa}$ and Young's modulus $E = 1.0\,\text{TPa}$ [35]. Graphene is then an extremely strong and stiff material. At the same time being a one atom thick layer, large sheets of graphene are flexible, express great elasticity and can withstand bending without breaking or rearrangement of atoms making them an interesting study subject for different kinds of flexible electronic devices.

The same strong in-plane σ-bonds are also responsible for graphene's unusually high in-plane thermal conductivity of $\kappa = 2000 - 4000\,\text{W/mK}$

[36] which is among the highest of any known material. Graphene however has relatively low out-of-plane thermal conductivity.

Discovery of graphene and the subsequent fundamental study of this 2D material has led to the discovery of other similar 2D materials similar in structure to graphene, but with distinctive properties, such as boron nitride [37]. These materials could be used in combination with graphene to develop new applications with properties that could be fine-tuned with different amounts of various 2D materials. Graphene is considered to be the perfect 2D material when it comes to eletrical properties, out of those discovered so far at least and these properties will be discussed next.

2.2.2 Electrical Properties

Graphene's extraordinary electrical properties stem from the out-of-plane π-bonds. The electron band structure they form can be differentiated as the valence band being the lower occupied π-band and the conduction band being the higher unoccupied π^*-band. Graphene is a so called zero band gap semiconductor meaning that it exhibits properties from both metals and semiconductors. Graphene is a zero band gap semiconductor because the conduction and valence bands touch only at the so called Dirac points where the energy gap is zero, and nowhere else, which differs considerably if compared to traditional semiconductors which have a finite band gap. Dirac points are points at the edge of the Brillouin zone as pictured in figure 2.5 and there are two sets of three Dirac points K and K' whose positions in momentum space are [32]

$$K = \left(\frac{2\pi}{3a}, \frac{2\pi}{3\sqrt{3}a}\right), \quad K' = \left(\frac{2\pi}{3a}, -\frac{2\pi}{3\sqrt{3}a}\right). \tag{2.2.4}$$

Dirac points and charge carriers of graphene (electrons and/or holes) around the Dirac points are of the most interest when considering electrical properties of graphene in comparison to normal semiconductors where usually Γ is the point of interest. The graphene charge carriers are also interesting because they change from electrons to holes at the Dirac point making it easy to study them compared to normal semiconductors where the electron and hole motion has to be studied by using differently doped materials. This phenomenon is called ambipolarity where charge carriers can be tuned between electrons and holes by supplying the correct gate bias.

Using the tight-binding model for electrons in graphene and assuming that electron hopping to both nearest- and second-nearest-neighbours is occuring, we can find the dispersion relation describing the energy bands [17, 32]. The following equations in this subsection use units such that $\hbar = 1$.

$$E_{\pm}(k) = \pm t\sqrt{3 + f(k)} - t'f(k), \tag{2.2.5}$$

where t and t' are the hopping energies respectively to nearest- and second-nearest-neighbours, the plus sign refers to the valence band π, the minus sign to the conduction band π^* and $f(k)$ is

$$f(k) = 2\cos\left(\sqrt{3}k_y a\right) + 4\cos\left(\frac{\sqrt{3}}{2}k_y a\right)\cos\left(\frac{3}{2}k_x a\right). \tag{2.2.6}$$

From these equations the band structure of graphene can be illustrated as shown in figure 2.6.

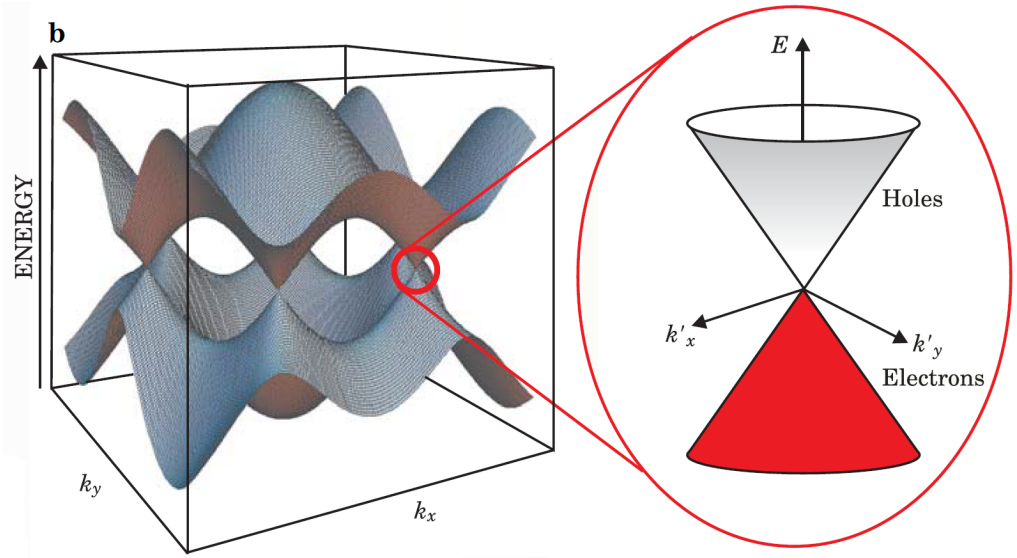

Figure 2.6: Band structure of graphene. Visible in the picture are the six Dirac points where the valence and conduction bands meet and a zoomed picture of the vicinity of one of the Dirac points. [38]

Looking at the zoomed picture of the band structure in figure 2.6 it can be seen that close to the Dirac points the energy-momentum dispersion relation is linear which acts as a basis for many of the interesting properties of graphene. This region can be described with the Dirac equation for massless fermions meaning that the mass of the charge carriers for graphene

near the Dirac points is effectively zero. This also separates graphene from normal semiconductors whose dispersion relation is quadratic and makes graphene so unique. Also usually Schrödinger equation is used to sufficiently describe electrical properties of different materials but not with graphene where the Dirac equation is more accurate. Dispersion for these graphene carriers in this linear region is

$$E_{\pm}(q) \approx \pm v_F|q| + O\left[\left(\frac{q}{K}\right)^2\right], \tag{2.2.7}$$

where $q = k - K$ and $v_F = 3t\frac{a}{2} \approx 1 \cdot 10^6\,\mathrm{m/s}$ is the Fermi velocity. Charge carriers in graphene behave like relativistic particles and these quasiparticles are called massless Dirac fermions. Dispersion in graphene is also chiral meaning that the carrier transport properties depend on the direction of propagation along the lattices also explaining why single-walled carbon nanotubes can be either metals or semiconductors depending on how they are wrapped. [17,32].

For pure graphene with no impurities or doping, the Fermi level E_F is equal to the energy at the Dirac point and there are only interband transitions between electrons and holes at low electron hopping energy because the conduction band is completely empty and the valence band is completely filled. For doped graphene the Fermi level will change away from the Dirac point and, e.g., n-doped graphene will have electrons also in the conduction band because the Fermi level will be higher and then intraband transitions can also occur. Interband transitions are transitions between electron/holes between the conduction/valence bands while intraband transitions are quantum mechanical interactions between levels within the conduction/valence bands. [32]

Graphene displays remarkable electron mobility with an incredibly high $\mu = 230\,000\,\mathrm{cm}^2/\mathrm{Vs}$ [39] measured at low temperatures and at ambient conditions $\mu = 15\,000\,\mathrm{cm}^2/\mathrm{Vs}$ [40] which is still several orders higher than traditional materials used in electronics. Electron and hole mobilities are also nearly identical which is usually not the case with other materials. Charge carrier densities in graphene can also be quite easily controlled by electrical gating and doping the material and this great tunability makes graphene interesting for various potential applications.

Another fascinating aspect of the electronic properties of graphene is the Quantum Hall effect (QHE). In Hall effect charge carriers moving inside a conductor are being exposed to a magnetic field perpendicular

to their normal propagation direction where the charges follow a path called line of sight between collisions with, e.g., impurities. The magnetic field curves their paths leading to charges accumulating on certain position inside the materials and therefore to an asymmetric charge density distribution which in turn leads to an electric field opposing the movement of carriers and a steady electrical potential is established. In QHE the Hall conductance σ_{xy} undergoes quantum phase transitions to take on the quantized values. QHE is exclusive to 2D materials and occurs in very low temperatures. Graphene is unique in that QHE is possible at room temperatures making these quantum effects more available for possible applications. [41]

2.2.3 Optical Properties

Graphene also exhibits unique optical properties. Despite being only one atom thick layer, in the near-infrared and visible region graphene has an optical absorbance of $\pi\alpha \approx 2.3\,\%$ where $\alpha = e^2/\hbar c \approx 1/137$ is the fine structure constant [42]. Absorbance of graphene therefore remarkably only depends on fundamental constants and not any properties of graphene and is also frequency independent which is not the case normally for materials. This is again due to the unusual band gap structure of graphene where the bands meet at the Dirac points and the Dirac fermions having a linear dispersion relation. This result of optical absorbance can be reached by looking at optical conductance σ_{uni} which is often used to describe optical properties of thin films. The Dirac fermions in graphene have universal conductance of [42, 43]

$$\sigma_{uni} = \frac{e^2}{4\hbar}. \tag{2.2.8}$$

Following from the Fresnel equations in the thin-film limit the transmittance can be expressed as

$$T = \left(1 + \frac{2\pi\sigma_{uni}}{c}\right)^{-2} = \left(1 + \frac{\pi\alpha}{2}\right)^{-2} \approx 1 - \pi\alpha \approx 0.977 \tag{2.2.9}$$

for the normal light incidence. Transmittance is then 97.7 % while the absorption is 2.3 % meaning that majority of the light passes through graphene but it can still be visible for the naked eye. Absorption coefficient of graphene in this region is about $7 \cdot 10^5\,\mathrm{cm}^{-1}$ when using a

thickness of 0.334 nm. Comparing this to GaAs for example, it is about 50 times higher than the absorption of GaAs at 1.55 µm wavelength, which is a clear evidence of the strong coupling between light and graphene. The reflectivity R of graphene is however extremely low. Only $R = 0.25\pi^2\alpha^2(1-A) = 1.3 \cdot 10^{-4}$ [44].

The optical conductivity of graphene in the far-infrared and terahertz region has a Drude form similar as for metals [44]

$$\sigma(\omega) = \frac{\mathrm{i}D_{gr}}{\pi(\omega + \mathrm{i}\Gamma)}, \tag{2.2.10}$$

where $D_{gr} = 2E_F\sigma_{uni}/\hbar$ is the Drude weight for graphene and Γ^{-1} is the damping rate.

The number of graphene layers in samples can be estimated by utilizing different optical measurements. Raman spectroscopy is commonly used to determine different materials within a sample and can be used to identify the number of layers of graphene. A more reliable and faster method could be simply to examine the transmittance through the sample since the transmittance is directly dependent on the optical conductance of the graphene stack and specifically in the visible region it can be estimated to be linearly proportional to the number of layers [45]. This method could be used for other 2D materials as well.

The optical transitions (interband and intraband) in graphene can be modified with electrical gating similarly as electrical transport properties can be changed with electrical gating which is not typical for materials. Interband optical transitions can be probed by using infrared spectroscopy and graphene has shown strong gate-induced changes in transition strengths because of the shift in Fermi level E_F due to gating which affects the interband transitions. This can be used to study the band structure of graphene in detail [46]. The gate-induced changes in the reflection strength in graphene can be seen in the infrared reflection spectra of graphene monolayer in figure 2.7. These optical transitions and the great tunability by electrical gating can lead to applications in infrared optics and optoelectronics.

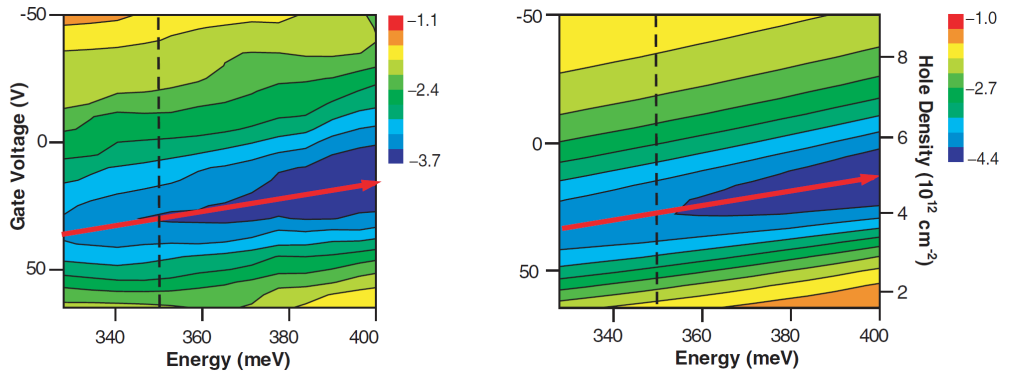

Figure 2.7: **a)** Two-dimensional plot of measured reflection spectrum $\partial(\delta R/R)/\partial V$ in graphene monolayer versus gate voltage and photon energy. The red line is the absolute value of $\partial(\delta R/R)/\partial V$ at which a fixed photon energy has a maximum at $V = V_{max}$ which varies with the photon energy. **b)** Calculated reflection spectrum. Calculations based on the tight-binding approximation. [46]

2.3 Surface Plasmons in Graphene

Graphene has emerged as a great alternative to traditional noble metals in producing surface plasmons because of its unique eletrical and optical properties and the subsequent relatively low loss, high confinement and great tunability of surface plasmons in graphene which will all be discussed in this chapter along with the dispersion relation and graphene nanodisks. Surface plasmon polaritons, i.e., plasmons coupled with photons are again the most common coupling type and the most interesting regarding possible applications but graphene can sustain plasmons coupling with phonons as well. The dispersion relation and the properties of surface plasmons in graphene will be discussed in this chapter along with graphene nanodisks.

2.3.1 Dispersion Relation

The dispersion relation for surface plasmons in graphene can be studied with different theories such as random-phase approximation, tight-binding approximation, first-principle calculation, Dirac equation continuum model and electron energy loss spectroscopy, but here a commonly

used semi-classical model is used. Most of the equations in this chapter are based on [47] and [48]. Graphene has a complex conductivity of

$$\sigma(\omega, \mu, \Gamma, T) = \sigma' + \mathrm{i}\sigma'', \tag{2.3.1}$$

where ω is the angular frequency, μ is the chemical potential, Γ is the charged particle scattering rate and T is the temperature. The conductivity can also be separated into intraband and interband transition parts

$$\sigma = \sigma_{intra} + \sigma_{inter}. \tag{2.3.2}$$

Intraband transitions can be expressed as

$$\sigma_{intra} = -\mathrm{i}\frac{e^2 k_B T}{\pi\hbar^2(\omega - \mathrm{i}2\Gamma)}\left[\frac{\mu}{k_B T} + 2\ln\left(e^{-\mu/k_B T} + 1\right)\right]. \tag{2.3.3}$$

For highly doped graphene $|\mu| \gg k_B T$ which leads to $e^{-\mu/k_B T} = 0$ and these intraband transitions can be then approximated to be

$$\sigma_{intra} = -\frac{e^2\mu}{\pi\hbar^2}\frac{\mathrm{i}}{\omega - \mathrm{i}2\Gamma} = \frac{e^2\mu}{\pi\hbar^2}\frac{\mathrm{i}}{\omega + \mathrm{i}\tau^{-1}}. \tag{2.3.4}$$

where $\tau = \mu_m \mu / e v_F^2$ is the electron relaxation time where μ_m is the carrier mobility.

Interband transitions in turn can be approximated as

$$\sigma_{inter} \simeq -\mathrm{i}\frac{e^2}{4\pi\hbar}\ln\left[\frac{2|\mu| - (\omega - \mathrm{i}2\Gamma)\hbar}{2|\mu| + (\omega - \mathrm{i}2\Gamma)\hbar}\right]. \tag{2.3.5}$$

Graphene can support both TE and TM surface modes leading to both types of SPs unlike in traditional materials. The modes are determined by the imaginary part of the conductivity where a negative imaginary part will lead to TE surface waves and a positive part to TM surface waves. TM mode is located in the THz and far-infrared regions while TE mode is located in the far-infrared and near-infrared regions. Intraband transitions contribute to TM mode and interband transitions contribute to TE mode. [47]

The dispersion relation for surface plasmons in graphene can be found by considering a simple situation of an infinite single-layer graphene situated at the interface between two different mediums characterized by

dielectric constants ϵ_r and ϵ_r'. From Maxwell equations the dispersion relation for TM mode can be found [49]

$$\frac{\epsilon_r}{\sqrt{k_{TM}^2 - (\epsilon_r \omega^2/c^2)}} + \frac{\epsilon_r'}{\sqrt{k_{TM}^2 - (\epsilon_r' \omega^2/c^2)}} + \frac{\mathrm{i}\sigma}{\omega \epsilon_0} = 0. \tag{2.3.6}$$

Considering isolated graphene where $(\epsilon_r = \epsilon_r' = 1)$, the dispersion relation for TM mode is

$$k_{TM} = k_0 \sqrt{1 - \left(\frac{2}{\sigma \eta_0}\right)^2}, \tag{2.3.7}$$

where $\eta_0 = \sqrt{\mu_0/\epsilon_0}$ is the intrinsic impedance of free space. The same steps can be done for TE mode and in isolated graphene the dispersion relation for TE mode is

$$k_{TE} = k_0 \sqrt{1 - \left(\frac{\sigma \eta_0}{2}\right)^2}. \tag{2.3.8}$$

Considering a situation where TM mode is dominating and graphene is highly doped on substrates where $\epsilon_r \neq 1$ and $\epsilon_r' = 1$, an analytical expression for the dispersion relation of SPs can be found [50]

$$k_{SP} \approx \mathrm{i}\epsilon_0(\epsilon_r + 1)\frac{\omega}{\sigma}. \tag{2.3.9}$$

Assuming TM mode is dominating means that the intraband transitions are dominating and equation (2.3.4) can be substituted into equation (2.3.9). Also assuming that $\mu \approx E_F$ because of $|\mu| \gg k_B T$, we obtain

$$k_{SP} \approx \frac{\pi \hbar^2}{e^2 E_F} \epsilon_0 (\epsilon_r + 1) \omega \left(\omega + \frac{\mathrm{i}}{\tau}\right). \tag{2.3.10}$$

From this the wavelength of surface plasmons in graphene can be found [47]

$$\lambda_{SP} \approx \lambda_0 \alpha \frac{4E_F}{\epsilon_r + 1} \frac{1}{\hbar(\omega + \mathrm{i}\tau^{-1})}, \tag{2.3.11}$$

where α is the fine structure constant. Typical wavelengths are around 200 nm [47]. The propagation distance can be found to be

$$\delta_{SP} \approx \lambda_0 \alpha \frac{\tau E_F}{\epsilon_r + 1} \frac{1}{\hbar(\pi + \mathrm{i}\tau^{-1})}. \tag{2.3.12}$$

Propagation distances can reach values well above 100 times higher than the surface plasmon wavelength [50].

2.3.2 Properties

The surface plasmon frequencies in metals are generally in the visible, near-infrared and near-ultraviolet region and the propagation distances for metals such as Au in this region are actually higher than for graphene [51] making graphene not as good of a material for SPs in this region. But for metals the loss of SPs increases dramatically when approaching the far-infrared and terahertz region due to the increased imaginary part of the dielectric function and due to the surface effect confining SPs in metals to the interface with the penetration depths of a few dozen nanometers. The penetration depth will increase rapidly when moving to far-infrared and THz region meaning significant loss of SPs in metals. However, this is not a problem for graphene in this region due to a smaller imaginary part of the dielectric function and penetration depth. [52] Also due to a relatively long optical relaxation. SPs in graphene experience much less loss, especially highly doped graphene.

The confinement of SPs can be estimated by the penetration depth. The penetration depths in graphene are clearly smaller than in metals resulting in higher confinement of SPs in graphene [52]. This is also apparent by looking at the effective SP index λ_0/λ_{SP} which for graphene is 40-70 while for metals it is relatively small [47]. As an example for 10 µm wavelength incident light with the graphene Fermi level being 0.15 eV and a relaxation time of $1 \cdot 10^{-13}$ s, the wavelength of surface plasmon in graphene on a SiO_2 substrate will be 155 nm and the subsequent SP index λ_0/λ_{SP} is 64 [44].

Tunability of graphene is the most interesting aspect of graphene plasmonics. SPPs can be tuned and controlled in metals by the structure but not after these structures are in place. Graphene can however be tuned by, e.g., changing the Fermi level or the chemical potential in room temperature which, as previously seen, affects the conductivity and dispersion relation of graphene with

$$E_F \approx \mu \approx \sqrt{\pi \hbar^2 v_F^2 n}, \tag{2.3.13}$$

where n is the carrier concentration which can be easily tuned by either electrical gating or chemical doping. Other ways to tune graphene SPPs can be done by substrates, magnetic fields or temperatures. Tunability of graphene allows much more precise control of SPPs than in metals. [47]

These three properties of relatively low loss, high confinement and great tunability of SPPs in graphene makes graphene plasmonics interesting for possible applications, especially in the infrared and THz region. For visible region SPPs in metals are superior in some ways but can be coupled with graphene to produce hybrid structures to enable better tunability.

The excitation of SPPs in graphene faces similar problems as within metals. There's a mismatch of momentum with the plasmons and incoming light. This can be solved through similar methods as with metals by using prisms, surface defects or periodic surface structures such as gratings as discussed in chapter 2.1.4. Other methods include a dipole emitter such as an excited molecule or a quantum dot.

Plasmons can also occur in different graphene nanostructures where localized plasmons play a major role and can be directly excited despite the momentum mismatch as discussed in chapter 2.1.4. These structures can include for example ribbons [53], disks [54], rings [55], and stacks [56]. Micro-/nanoribbons are one of the most studied out of these. In them, by reducing the degree of freedom by having only a ribbon of certain width, SPP propagation direction can be controlled while the local surface plasmon resonance is enhanced because of the confinement in other directions. These ribbons could be used for example as wave guides. Nanodisks are the most interesting subject regarding this thesis, however, and will be discussed next.

2.3.3 Graphene Nanodisks

The dimensionality can be reduced even further from ribbons into disks. The zero-dimensional nature of disks makes localized surface plasmon resonance in these nanostructures even more powerful causing a strong enhanced electrical field. The EM field in graphene disks behaves like a dipole, similarly as in metal nanoparticles where the disks have a perceived positive charge on one side of the disk and a negative charge on the other side. [47] A simple illustration of a graphene nanodisk array can be seen in figure 2.8.

The optical conductivity of an array of disks is [44,54]

$$\sigma(\omega) = \mathrm{i}\frac{fD_{gr}}{\pi}\frac{\omega}{(\omega^2 - \omega_p^2) + \mathrm{i}\Gamma_p\omega}, \tag{2.3.14}$$

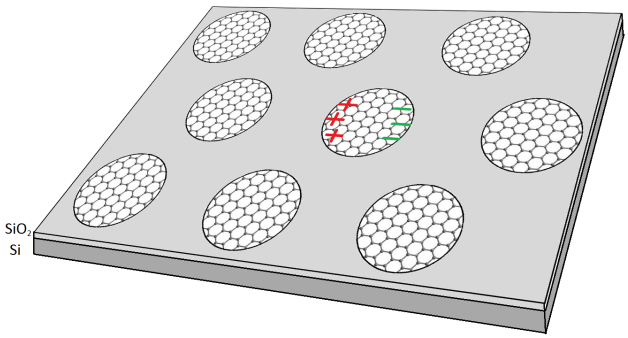

Figure 2.8: A simple illustration of a graphene nanodisk array on a Si/SiO_2 substrate schematically showing also the dipole oscillation in one nanodisk.

where f is the filling factor as in the fraction of the surface occupied by the graphene disks, D_{gr} is the Drude weight and Γ_p is the plasmon resonance width. The localized plasmon frequency is

$$\omega_p = \sqrt{\frac{3D_{gr}}{8\epsilon_m\epsilon_0 d}}, \tag{2.3.15}$$

where ϵ_m is the dielectric constant of the medium and d is the disk diameter.

The plasmons in graphene can couple with phonons in polar insulator materials like SiO_2 where surface phonons are present and extend above the surface of the substrate. Phonons are collective excitations of the vibrational states. This results in hybrid excitation modes of plasmons and phonons, the energies and strengths of these modes determined by the corresponding plasmons and phonons. Phonon lifetimes are much longer than plasmon lifetimes thus making the hybrid mode lifetimes much longer. These plasmon-phonon interactions are therefore interesting when considering, e.g., large-scale nanodisk structures which is necessary for possible applications. [44] The SP coupling within the nanostructures on the same plane between nanodisks for example, is relatively low but much higher for stacked structures [47].

Electrically doping nanostructures such as nanodisks by using an external electric field, i.e., gate voltage can shift the energies and strengths of the plasmons as seen in figure 2.9 where the electrical and geometrical tuning of the dipolar plasmons in nanodisks can be controlled easily. In

figure 2.9a it can be clearly seen from the measured extinction spectra that for a fixe sized nanodisk the photon energy increases with the increased doping, i.e., gate voltage and in figure 2.9b it can be clearly seen that with a constant doping level the photon energy increases when the disk diameter decreases. The results are confirmed by the different theories seen as either the dashed curves calculated from local RPA and the dotted curves calculated from Drude such as equations (2.3.4) and (2.3.5). [24]

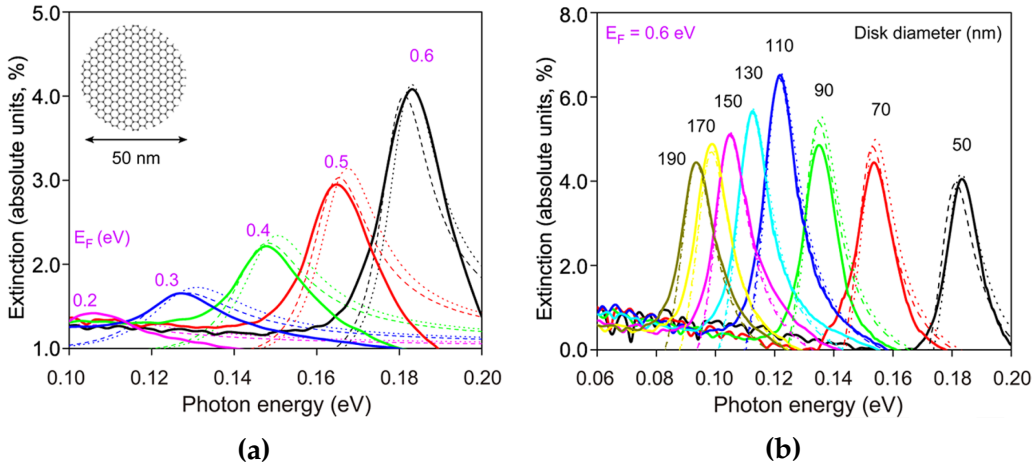

Figure 2.9: **a)** Extinction spectra of a 50 nm graphene nanodisk array under different applied gate voltages ΔV quantified through the Fermi level E_F. Solid curves = measured, dashed curves = calculated from local RPA, dotted curves = calculated from Drude. **b)** Extinction spectra of a graphene nanodisk array with different disk diameters under fixed doping $E_F = 0.61$ eV. Showing again the measured and calculated curves. [24]

Localized plasmons in graphene decay primarily by producing electron-hole pairs which can be beneficial for potential applications. The unusually high light confinement of plasmons in graphene can be seen from figure 2.9 where, e.g., a photon energy of 0.15 eV corresponds to a far-field wavelength of approximately 8.27 µm which is several dozens or even over 100 times larger than the size of the nanodisks. This can lead to potential applications as well. [24]

3 Experimental Methods and Results

The understanding and utilization of various nanofabrication methods is crucial when studying nanotechnology such as surface plasmons and graphene. Different kinds of lithography methods are commonly used to manufacture structures and patterns on the nanoscale. Lithography methods in general will be discussed in this chapter and the various steps and the machinery needed to make them work. The experiments and the results will also be discussed. The aim of the thesis was to modify the hole-mask colloidal lithography method [25] to find a fabrication method that would result in a desired pattern of randomly organized graphene nanodisks with a good amount of the sample covered. The studied fabrication steps and parameters and the final fabrication method will be discussed next. Also discussed will be the measurements tried on these graphene nanodisk samples with a FTIR spectroscope. The aim was to see similar results as [24] where surface plasmons in graphene nanodisks will shift in energy and strength by changing the gate voltage.

3.1 Lithography Methods and Machinery

Different kinds of lithography methods can be categorized in many ways whether they are for example resist-based or not, beam or tip-based, top-down or bottom-up, or mask-based or not. Examples of commonly used methods include photolithography, electron-beam lithography, nanoimprint lithography, molecular self-assembly, and nanosphere lithography. Photolithography and electron-beam lithography are the dominant methods and the related steps will be discussed next. They are also good examples of top-down approaches where externally controlled tools are used to create desired patterns on samples while molecular self-assembly is an example of a bottom-up approach where the chemical properties of molecules are utilized to cause them to self-organize or self-assemble into desired patterns.

3.1.1 Resists and Spin Coating

The surface of the sample is first coated with a thin film of resist material. Resists used depend on the lithography method in question but usually

contain various polymers, a solvent, and a radiation sensitive component. In the case of photolithography, resists are light-sensitive. Resists act as a medium on which the desired pattern will be deposited and protect the underlying substrate at the same time. Commonly used resists in photolithography are, e.g., AZ or SU-8 and for many other purposes polymethyl methacrylate (PMMA). A small amount of resist is applied on the sample which is then rotated at a high speed for a set amount of time in a spinner, hence the name spin coating. The centrifugal forces will spread the resist evenly across the sample and result in a thin film which is then heated for a small amount of time to achieve a solid thin film by removing excess solvent. The thickness of the film can be adjusted with the spinning parameters and viscosity of the resist, i.e., the amount of the solvent. [57, p. 107-117]

3.1.2 Exposure and Development

Resist is then exposed to ionizing radiation, in the case of photolithography, UV-light. This exposure causes chemical changes in the polymers inside the resist. Masks are used to create patterns on the sample by exposing just some part of the resist to radiation. Resist can then be removed by developing it in a special solution. Resists can be either positive or negative depending on whether the exposed part of the resist is removed during the development or the untouched part is removed. Positive resist becomes soluble in the exposed area due to chain breaking inside the resist and negative resists in the unexposed area due to cross-linking of chains inside the resist in the exposed area. Usually after the next steps, etching and evaporation or similar, a lift-off procedure is done to finalize the sample. In lift-off all of the remaining resist is removed, for example, in heated acetone to achieve the final pattern. [57, p. 107-117]

3.1.3 Etching

Etching can be used to remove layers of materials, including substrates and resists, from the samples. Etching can be categorized into wet and dry etching methods. Wet etching uses liquid etchants and dry etching uses plasma. Wet etching resembles the development part of the resist removal but with etching all kinds of materials can be removed. Wet etching is usually isotropic meaning that they will not produce clear ver-

tical walls when etching and will undercut materials resulting in round walls. Highly isotropic etchants etch the material equally in all directions. This is why dry etching is preferred because of its better anisotropy possibilities even though some wet etchants can have great anisotropy as well. Anisotropic processes produce much better controlled features which is why it is often the preferred method. The depth of etching can be controlled by the etching time when knowing the etching rates of different etchants into different materials. Etching can also be done to clean the sample, for example, of some possible left over resist. [57, p. 121-131]

Reactive ion etching (RIE) is a commonly used dry etching process with great anisotropy where plasma-enhanced chemical reactions are utilized. The sample is placed in a vacuum chamber with reactive gas at a low pressure on an electrode coupled to a radio frequency (RF) source. Plasma is created by applying an RF electromagnetic field where the oscillating electric field ionizes and excites the gas. Ion bombardment towards the sample leads to enhanced chemical reactions with the ions and the excited species resulting in etching. [57, p. 121-131]

3.1.4 Evaporation

Evaporation is a simple method of depositing at thin film of material onto samples to create desired patterns. A source material is heated with, e.g., an electron beam or a resistive heater in a vacuum. Evaporated particles travel straight onto the sample without any collisions because of the vacuum, resulting in a uniform layer of material deposited and only on the parts that are visible from the source point. Particles condense when arriving on the sample to form a solid layer. Often times various metals are used when evaporating but other materials like insulators can be used as well. Evaporation can be done in high vacuum with pressures of $1 \cdot 10^{-3} - 1 \cdot 10^{-7}$ mbar or ultra high vacuum (UHV) where pressures are lower than $1 \cdot 10^{-7}$ mbar. Ultra high vacuum allows for even more precision and uniformity with less impurities in the deposited thin film. The thickness of the deposited layer can be monitored with the help of a Quartz Crystal Microbalance (QCM) which has a very precise resonance frequency that is extremely sensitive to changes in its mass. [57, p. 49-50]

3.1.5 Scanning Electron Microscope

The basic components of a scanning electron microscope (SEM) can be seen in figure 3.1. An electron gun is used to produce electrons. Electrons can be produced in several different ways, e.g., thermionic emission, Schottky emission and field emission. These electrons then go through different types of magnetic lenses that focus the beam of electrons by magnetic field. As the electrons pass through the magnetic field they start to spiral through the lens and then start to focus on desired position. The magnetic field is inhomogenous so electrons further from the middle of the beam are more strongly deflected with the overall effect being that the electron beam can be focused precisely into one spot. These lenses also allow SEM to have an unusually high depth of focus compared to optical microscopes. [58, p. 21-24]

Another important part of the components in SEM are the electron detection systems which are responsible for forming the image. When the sample is hit with an electron beam different kinds of scattered electrons are formed as seen in the right side of figure 3.1. The most important are the secondary electrons which are electrons knocked out from atoms by inelastic collisions with the primary beam electrons. These electrons carry important information about the surface structure of the sample because they have low energies and only come from very near the surface. SEM is therefore an excellent tool to study the surface structures of materials. Backscattered electrons are another detected electron form which are elastically scattered primary electrons roughly in the opposite direction of the electron beam. These come from much deeper from the sample than secondary electrons and have higher energies. Other detection methods that are not quite as meaningful include X-ray emission which is unique to every element and can be used to identify different elements in the sample. Auger electrons, cathodoluminescence, and absorbed electrons resulting in absorbed current can be studied as well. [58, p. 21-24]

Scanning electron microscope is an excellent imaging tool with many advantages over optical microscopes. When using, for example, an acceleration voltage of 40 kV for the electrons, the theoretical wavelength of electrons can be calculated which is five orders of magnitude smaller than the wavelength of light. Resolution limiting factors with SEM are, for example, different spherical and chromatic aberrations. Other problems with SEM include that the sample needs to be electrically conductive and

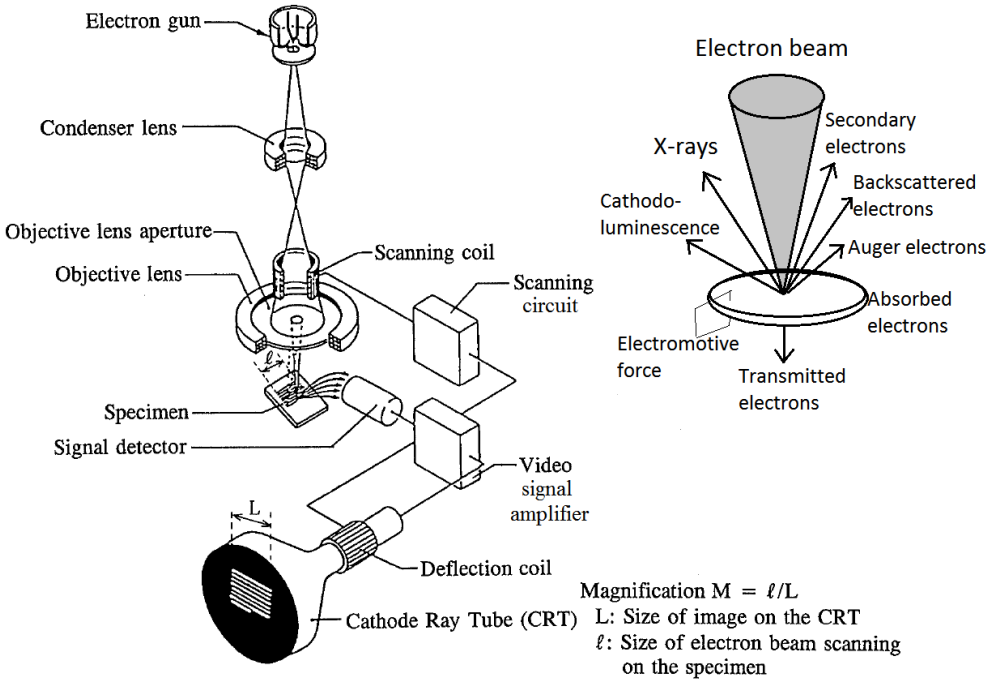

Figure 3.1: The basic components of a scanning electron microscope and the different detected electrons. [59]

samples not naturally conductive have to be coated with a thin layer of, e.g., gold. Otherwise the electrons would charge the sample, resulting in imaging artifacts. A good vacuum is also important to avoid unnecessary collisions of electrons with gas and particles and to prevent beam-induced deposition.

In addition to SEM being an excellent imaging tool it can also be used to perform electron beam lithography (EBL). The principle is similar to photolithography but in EBL the resist is exposed in desired areas with the concentrated electron beam and parts of the resist can then be removed depending on the resist used. In EBL the exposure is done point by point which makes it extremely slow for larger areas compared to photolithography.

3.1.6 Atomic Force Microscope

Atomic force microscope (AFM) is another great tool for imaging samples. The basic components of an AFM can be seen in figure 3.2. The sur-

face of the sample is probed by using a sharp tip attached to a flexible cantilever. The tip radius is usually on the scale of only a few nanometers to few tens of nanometers. The interactions and the distance between the tip and the surface is measured and kept constant by modifying the height position of the sample. Laser is pointed at the cantilever that moves with the deflections caused by the interactions between the tip and the surface and the reflection of the laser is measured with a photodetector which will provide the necessary information to form an image. This signal is run through a feedback loop also seen in figure 3.2. The error signal obtained from the feedback loop indicates the amount that the position of the sample needs to be adjusted in order to maintain the constant force and distance between the tip and the surface. The position of the tip and the sample is adjusted with the help of piezoelements. [60]

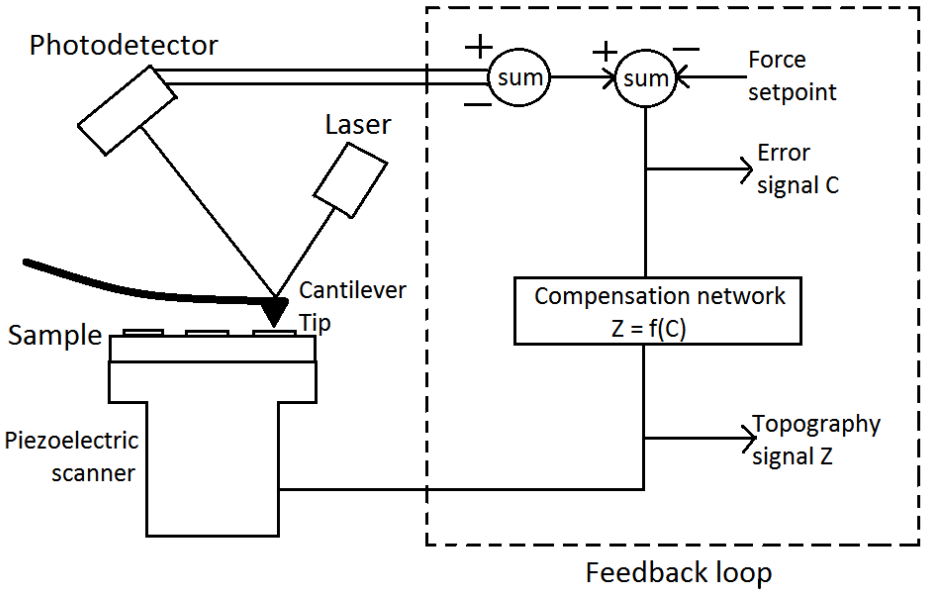

Figure 3.2: The basic components and the feedback loop of an atomic force microscope.

AFM can be operated in different modes depending on the tip motion. In contact mode the tip is in contact with the sample resulting in excellent resolution but possibly damaging the sample. In non-contact mode the tip is made to oscillate just above the sample. This will still allow forces to be measured but will keep the sample and the tip intact. Tapping mode is the most common one nowadays where again the tip is made to oscillate

but with a higher amplitude that might result in the tip making contact with the sample. This will result in better results but again might damage the sample and the tip, far less though than contact mode. [60]

AFM is an excellent tool for studying the topography of samples but also other surface features such as those manufactured by lithography methods. It is also an extremely accurate tool, in the nanometer scale because of the sharpness of the tip.

3.1.7 Hole-Mask Colloidal Lithography

Different colloidal lithography (CL) methods have been developed to produce large-scale two-dimensional arrays of various nanostructrues with the help of colloidal spheres. These methods are so called bottom-up methods where molecules self-organize or self-assemble into desired patterns due to, e.g., chemical properties. Nanosphere lithography (NSL) is an example of a commonly utilized colloidal lithography method. In NSL, self-assembled 2D colloidal crystals in a hexagonally close-packed lattice are used as an evaporation mask where evaporation through the holes between the nanospheres results in a desired pattern which can be modified depending on, e.g., evaporation angle or deposition method of materials. [25]

Another example of a colloidal lithography method is sparse colloidal lithography (SCL). Here charged polystyrene (PS) nanospheres are utilized in a similar way as in NSL. A sparse layer of PS nanospheres is created and used as an evaporation/etching mask. This enables relatively easy production of large-scale nanostructures of even several cm^2 to be fabricated with different patterns such as disks, rings, and holes. Overall sizes of the structures manufactured can be down to 20 nm and the structures occupy $10 - 50\,\%$ of the total surface area. Problems occur with this method however with certain materials and etching selectivity where etch rates of the substrate or PS compete with the etch rate of the actual material. Also the removal of the PS sphere mask is done through reactive oxygen treatment and certain materials prone to oxidation will deteriorate because of that. [25]

An improved version of SCL where the problems mentioned have been addressed is called hole-mask colloidal lithography (HCL). In HCL the principle is very similar to SCL but now a new sacrificial resist layer is

added to the process combined with the layer of polystyrene spheres. The sacrificial layer is added to protect the materials underneath and to help with the removal of the PS spheres. [25]

The basic fabrication steps in HCL start with spin-coating a thin layer of PMMA onto the sample. A short oxygen plasma RIE etch is then performed to improve the hydrophilicity of the PMMA layer so that the attachment of the PS spheres is easier. A charged polyelectrolyte polydiallyldimethylammonium (PDDA) suspended in water is then pipetted onto the sample to cover the surface. This forms a thin adhesive layer on the surface of the polymer. Then the colloidal solution of PS spheres is pipetted onto the surface. The PS spheres are charged oppositely compared to the previously deposited polyelectrolyte layer. Electrostatic repulsion between the PS spheres keeps the spheres apart from each other while the electrostatic attraction between the different layers keeps the spheres attached to the surface. The oppositely charged PDDA layer also masks the repulsion between the PS spheres enabling the control of the amount of spheres on the surface by changing the amount of PDDA used. A higher concentration of PDDA means a more closely packed layer of PS spheres. [25]

The surface is then dried with nitrogen flow to rapidly remove the colloidal solution to avoid rearrangement of the colloids. A thin film of oxygen plasma RIE resistant material, usually gold, is deposited onto the surface. The PS spheres are then stripped away using tape. This leaves holes in the plasma-resistant layer on top of the PMMA layer hence the name hole-mask colloidal lithography. RIE is then used to remove the PMMA inside the holes exposing the sample underneath for further processes. This mask can now be used for etching or evaporation purposes, e.g., to evaporate material onto the sample leading to disks the size of the holes. The excess PMMA and plasma-resistant layer can then be removed with lift-off, resulting in the desired nanostructured pattern which can be modified by evaporation angle or etching rates etc. [25] A diagram of the different HCL process steps is shown in figure 3.3.

Overall hole-mask colloidal lithography nanofabrication method allows large area coverage with relative ease, high fabrication speed independent of the surface area, and control over pattern size and spacing.

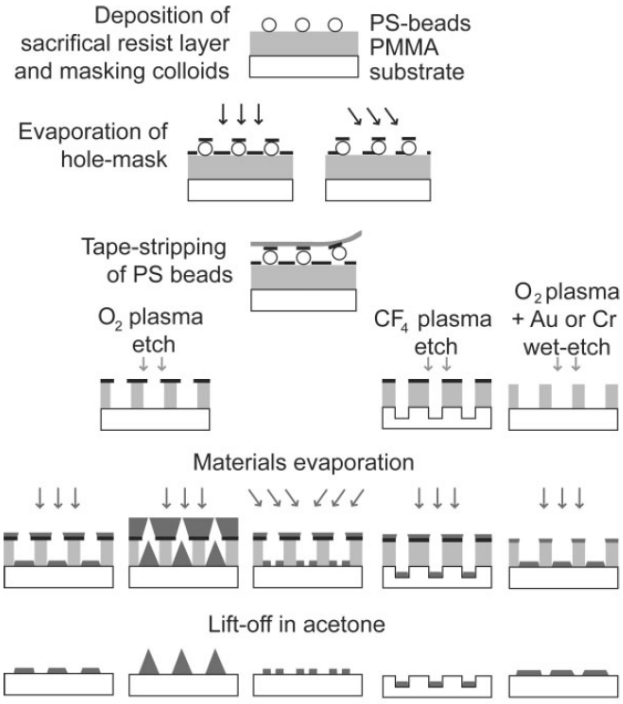

Figure 3.3: A diagram of the different HCL process steps with different kinds of patterns depending on the etchant used, evaporation angle or evaporation rate. [25]

3.2 Sample Fabrication

To start off the process of developing the fabrication method ideal for the desired graphene nanodisk samples for this thesis, firstly polystyrene spheres alone were deposited on silicon chips to be looked at with a scanning electron microscope. The silicon chips used throughout the experiments here were always cleaned at the start before doing any fabrication steps by sonicating them in hot acetone for 5 min and then sonicating in isopropyl alcohol (IPA) for 5 min after which it was dried with a N_2 flow. This is done to remove any impurities from the silicon chips.

The PS spheres were deposited onto the silicon chips by first adding a thin adhesive layer of positively charged polyelectrolyte. This was done by using PDDA solution (0.2 wt% in de-ionized water). PDDA was pipetted onto the sample to cover the surface, left there for 30 s to allow as much of the PDDA to attach to the surface as possible, then rinsed with de-ionized water under a moderate stream for 30 s. After that the sur-

face was dried by gently pressing a piece of paper on the sample. If the surface is wet then the PS spheres would not be able to attach properly. The negatively charged PS sphere solution (0.2 wt% in de-ionized water) was then pipetted onto the sample and left there for 2 min then rinsed for 1 min similarly with de-ionized water and again dried similarly with paper. The PS spheres were 200 nm in diameter and will be in all of the future samples where needed unless otherwise mentioned. The results can be seen in figure 3.4 taken with a scanning electron microscope (Raith eLine). In 3.4a a large area of PS spheres can be seen but most of them are bunched up together which is not what we want. In 3.4b an area with very few spheres can be seen. This is a common sight with this method since the deposition method, rinsing, and drying are not ideal and will often lead to areas where the spheres or PDDA have been, e.g., rinsed off or for some other reason have not attached well to the surface and because of these the samples often have different kind of areas with different concentrations of spheres.

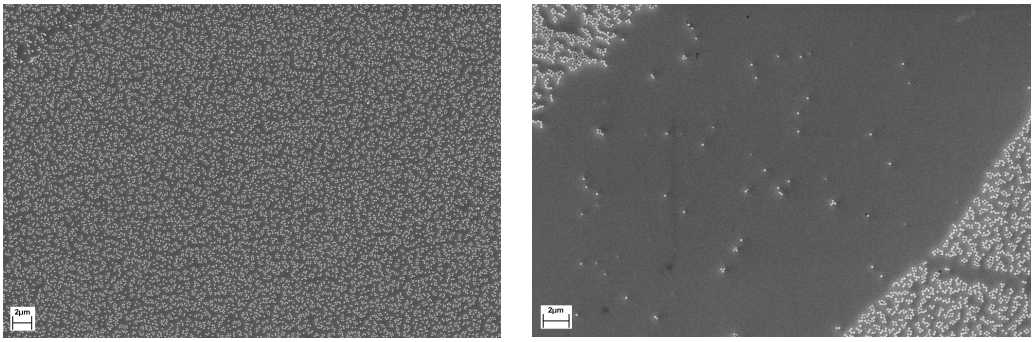

(a) **(b)**

Figure 3.4: a, b) SEM images of PS spheres (0.2 wt%, 200 nm, PDDA 0.2 wt%) on a silicon chip.

After this very simple test to see how the spheres look like on just silicon chips, different parameters were started to be tested and studied.

3.2.1 Optimizing the PDDA Concentration

Different PDDA weight percent solutions were tested to see what kind of effect they have and to hopefully find a way to separate the spheres as opposed to figure 3.4a where majority of them have attached in clusters. The sphere parameters were the same as in the initial test and silicon

chips were used but now PDDA 0.4 wt% was used with result shown in figure 3.5a and PDDA 1.0 wt% was used with result shown in figure 3.5b. The difference compared to 3.4 is really not that apparent. It appears though that with increased PDDA, the spheres attach even more into clusters. This was however difficult to determine because as explained above, there are different areas in the samples with different concentrations of spheres. With increased positive charge on the surface due to the increased amount of PDDA leads to more clusters of negatively charged PS spheres as explained previously in chapter 3.1.7. Based on these experiments it was determined that smaller weight percent solution of PDDA yielded better results so 0.02 wt% PDDA was chosen for the final process.

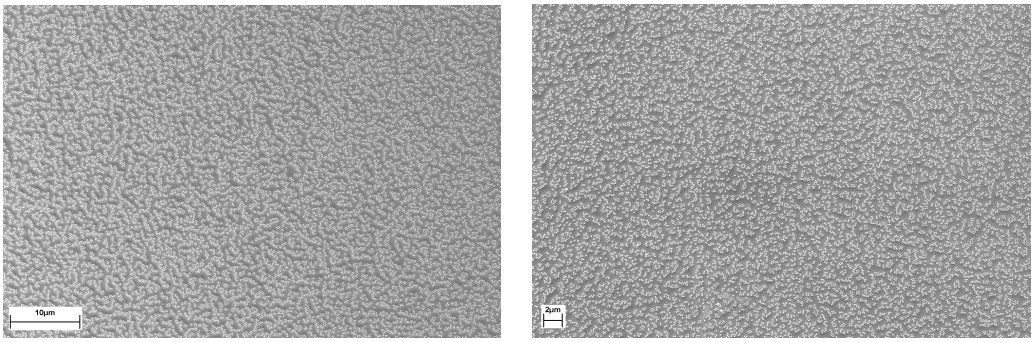

(a) **(b)**

Figure 3.5: a) SEM image of PS spheres (0.2 wt%, 200 nm, PDDA 0.4 wt%) on a silicon chip. **b)** SEM image of PS spheres (0.2 wt%, 200 nm, PDDA 1.0 wt%) on a silicon chip.

3.2.2 Checking the Necessity of Hydrophilic PMMA

PMMA was used to create a thin layer of resist on top of the silicon chips and then the PS spheres would be deposited on top of the PMMA layer. Resist was spin coated with a spinner (Bidtec SP-100). 495 PMMA A2 in anisole was used where 495 refers to the molecular weight of the PMMA and A2 refers to the amount of anisole in the solution (2 % in this case). 495 PMMA A2 was used in all of the future samples where PMMA was needed unless otherwise mentioned.

Approximately 80 nm of PMMA was deposited on a silicon chip in a spinner at 2000 rpm for 60 s after which the sample was baked on a hot plate of around 150 °C for 5 min. Another exactly similar sample was made with

80 nm of PMMA on a silicon chip. The second sample was made more hydrophilic with RIE (Oxford Instruments: Plasmalab 80 Plus) with an extrasoft O_2 plasma process (15 W, 30 mTorr, 10 s, O_2 50 sccm). PS spheres were then deposited on both samples by first adding PDDA (0.2 wt%) again to the surfaces, left there for 30 s, rinsed for 30 s and dried with paper. PS spheres (0.2 wt%) were added to the surfaces, left there for 2 min, rinsed for 1 min and dried with paper. The results can be seen in figure 3.6. It was clear that the deposition method needs the RIE step to make PMMA more hydrophilic to better allow the PDDA and spheres to be attached.

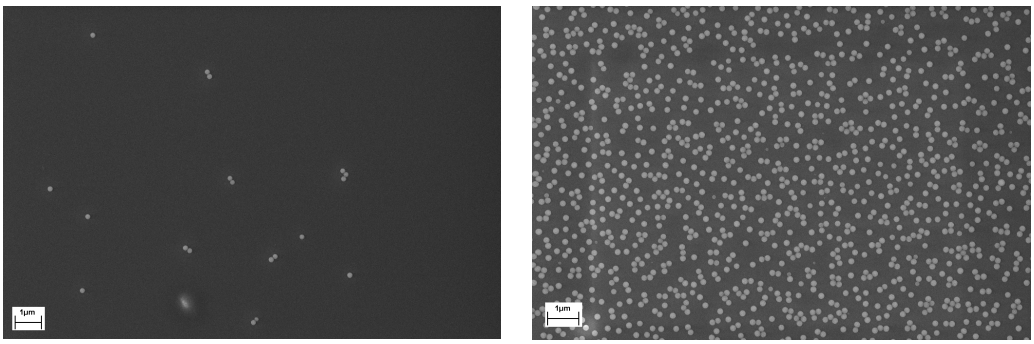

(a) **(b)**

Figure 3.6: a) SEM image of PS spheres (0.2 wt%, 200 nm, PDDA 0.2 wt%) on a silicon chip with 80 nm of PMMA. **b)** SEM image of PS spheres on a similar silicon chip where the PMMA was made more hydrophilic with a short RIE O_2 plasma etch.

3.2.3 Optimizing the PS Sphere Concentration

The concentration of PS spheres was studied by testing 0.02 wt% and 2 wt% solutions of PS spheres instead of the previously used 0.2 wt%. Also 80 nm of PMMA seemed a bit too much so the thickness was lowered to 50 nm by spinning at 3500 rpm for 45 s. The deposition was again exactly the same with the O_2 RIE etch, 0.02 wt% PDDA using N_2 drying and either 0.02 wt% or 2 wt% PS spheres. The results can be seen in figure 3.7. Both of these seem better than 0.2 wt% PS spheres because there are less clusters. With 0.02 wt% there are maybe a bit too few of the spheres present.

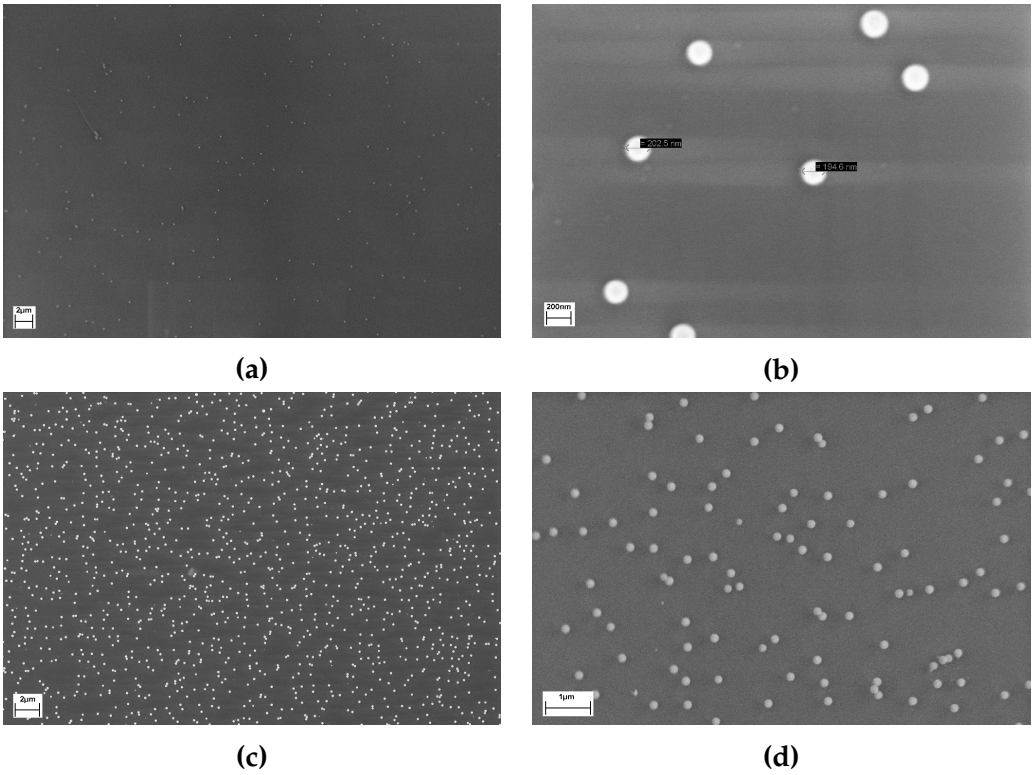

Figure 3.7: a), **b)** SEM images of PS spheres (0.02 wt%, 200 nm, PDDA 0.02 wt%) on a silicon chip with 50 nm of PMMA. **c)**, **d)** SEM images of PS spheres (2 wt%, 200 nm, PDDA 0.02 wt%) on a silicon chip with 50 nm of PMMA.

3.2.4 Testing Different Drying Methods

Different types of paper drying methods were tried with exactly the same sphere and PDDA parameters on a silicon chip. The drying was done by, e.g., just placing the paper on top of the sample and let it soak up the excess solutions or very gently pressing the paper on top of the sample or on the corner of the sample to dry it, and also with slightly different times to keep the paper on the sample. The results were again looked at with SEM but any substantial differences could not be detected.

Another drying method was tested next: drying with a nitrogen N_2 flow. Compared to the previously used paper drying method not too much of a difference was noticed as was with the different paper drying methods. However looking at the area distribution of PS spheres, it seemed that

N_2 drying resulted in more of the surface area covered with PS spheres which is of course desirable. N_2 drying also felt like a more reliable method because there is no need to have contact with the sample as with drying with paper. Problem could be that the N_2 flow is so strong that it detaches some PS spheres but in the end that did not seem to be an issue so N_2 flow was chosen to be used in the process instead of paper to dry the samples.

3.2.5 Testing the Etching Parameters

For the final samples we don't want any PMMA left in the samples so we need to perform some etching experiments to find out how to best remove all of the PMMA. This was tested by first manufacturing many samples this time with 0.02 wt% PS spheres but otherwise similar steps as before. After that a more powerful RIE etch was performed with O_2 plasma process (250 W, 15 mTorr, 30 s, strike pressure 50 mTorr, O_2 50 sccm, Ar 50 sccm). This was done to hopefully remove all of the unnecessary PMMA from everywhere but underneath the deposited PS spheres. Very low pressure was chosen to enhance ion bombardment and thus the anisotropicity of the etch, which better leaves the areas under PS spheres intact. After which a thin layer of 20 nm of titanium was evaporated with a UHV evaporator. Finally a lift-off procedure was done in hot acetone to remove the rest of the PMMA if it had not been etched away already. The sample was then looked at with SEM. If the RIE etch had etched away all of the PMMA, then the sample should be covered in Ti but if the etch was not powerful enough, then the evaporated Ti would have been on top of the PMMA that was not etched away and would be removed from the sample during the lift-off when removing the PMMA underneath the Ti.

Some results can be seen in figure 3.8. In 3.8b the lighter part on the top right corner of the sample is from the sample holder used in evaporation. That part of the sample was therefore not exposed to Ti and had only PMMA which was removed during lift-off. It can be clearly seen how the rest of the sample is covered in titanium meaning that the etch was powerful enough to remove all of the PMMA. In 3.8a there are holes in the sample where you can see the silicone underneath and rest of the sample is covered in titanium so the etch was powerful enough.

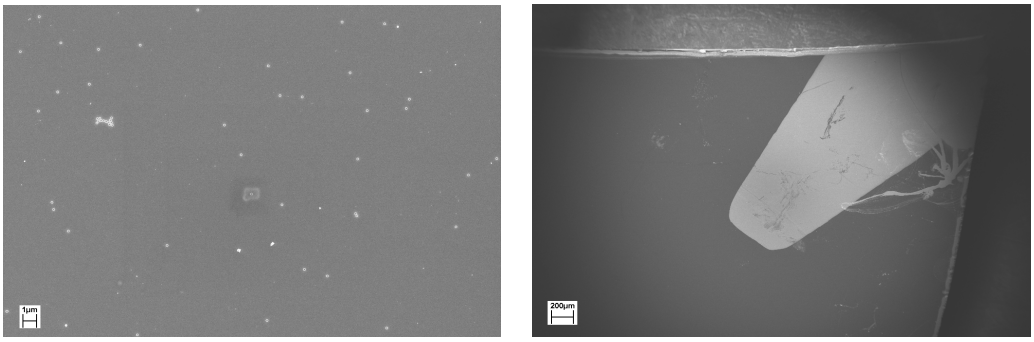

(a) **(b)**

Figure 3.8: a, b) SEM image of PS spheres (0.02 wt%, 200 nm, PDDA 0.02 wt%) on a silicon chip with 50 nm of PMMA etched away with a powerful RIE O_2 plasma etch and 20 nm of Ti evaporated and finally lift-off procedure done.

However, the etching was most likely too powerful which is not what we want. For the final process it would be ideal that the etch only removes the 50 nm of PMMA and stops at that and not try to etch away too much of the sample underneath the PMMA. Therefore experiments were made to test out different etching parameters. Mainly the etching time but also the strike pressure was lowered. The same strategy was used to see at what point the Ti layer was removed along with the leftover PMMA if the etch was not long enough. It was found that around 7 to 8 s would be the ideal etching time with a strike pressure of 30 mTorr.

Also multiple experiments were performed regarding melting the PS spheres on the samples in an oven at different temperatures and for different times and at various points during the other experiments mentioned earlier. The point was that melting the spheres would help with the possible isotropicity of the etching process. If the spheres are melted, it would be more difficult for the etching process to undercut samples and etch away the underlying material beneath the spheres because if the spheres are intact, they are only touching the surface a little and would enable the undercut. This wasn't very successful though and did not yield good results since the PS spheres mostly melted too much and it seemed like the etching process was anisotropic enough that this was not a problem in the end.

3.2.6 Testing with Graphene Samples

After most of the experiments for the fabrication steps were made, samples of graphene were started to be studied. Graphene samples were bought from Graphenea and the graphene was on a SiO_2/Si substrate. A SEM image and an AFM image of one graphene sample can be seen in figure 3.9.

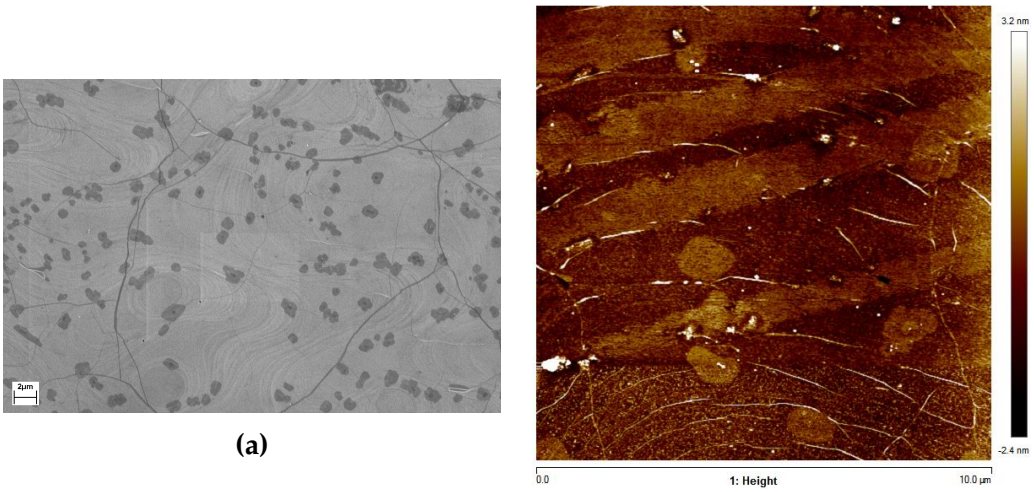

(a) **(b)**

Figure 3.9: a) SEM image of a graphene sample on a SiO_2/Si substrate. The surface is filled with a monolayer of graphene. The darker spots are areas where there are more layers of graphene. **b)** AFM image of a graphene sample on a SiO_2/Si substrate. Some impurities can be seen in the sample.

For graphene samples, the previously perfected fabrication steps were then performed. Firstly 50 nm of PMMA was spin coated onto the surface after which the extrasoft O_2 RIE etch (15 W, 30 mTorr, 10 s, O_2 50 sccm) was carried out. 0.02 wt% PDDA was then deposited onto the surface, left there for 30 s, rinsed with de-ionized water for 30 s and dried with a N_2 flow. 0.02 wt% PS spheres were used, left there for 2 min, rinsed for 1 min and dried with N_2. A powerful O_2 RIE etch (250 W, 15 mTorr, 7 s, strike pressure 30 mTorr, O_2 50 sccm, Ar 50 sccm) was then performed to etch away the PMMA and graphene from everywhere but under the PS spheres. Images of the sample were taken at this point to see how well the process worked on an actual graphene sample. Then the PS spheres were attempted to be removed with tape and the sample was imaged after this

as well. Finally the sample was left overnight in acetone after which the possible rest of the spheres and PMMA was tried to be removed in hot acetone and rinsed with IPA and images were taken in the end also. This should give us a sample of randomly organized 200 nm graphene disks.

SEM images from different stages can be seen in figure 3.10 and AFM images in figures 3.11, 3.12, and 3.13. From looking at the sample with AFM it still perhaps looked like not all of the graphene was removed during the etch so for the final fabrication the etching time was increased a bit. From the height profiles it can be clearly seen how removal with tape was able to successfully remove at least some of the spheres and the final removal with acetone removed the rest of the PMMA. There was however some leftover residue PMMA on top of the graphene disks still. There were quite a bit of impurities in the sample, perhaps from the use of acetone but it could be due to many reasons. Also there seemed to not be enough of the PS spheres so a higher concentration solution should be used.

3.2.7 Final Fabrication Steps

After some slight adjustments the final fabrication steps were used to manufacture graphene nanodisk sample on graphene on a SiO_2/Si substrate bought from Graphenea as seen in figure 3.9. Firstly 50 nm of 495/A2 PMMA was spin coated (3500 rpm, 45 s) onto the surface. The extrasoft O_2 RIE etch (15 W, 30 mTorr, 10 s, O_2 50 sccm) was performed to make the surface of the PMMA more hydrophilic to better allow attachment of PDDA and PS spheres.

A thin adhesive layer of polyelectrolyte PDDA was deposited onto the surface by covering the surface with 0.02 wt% PDDA, left there for 30 s, rinsed under a moderate stream of de-ionized water for 30 s and dried carefully with a N_2 flow. PS spheres were then deposited onto the surface by covering the surface with 2 wt% 200 nm PS spheres, left there for 2 min, rinsed again under a moderate stream of de-ionized water for 1 min and dried with N_2. A more powerful O_2 RIE etch (250 W, 15 mTorr, 8 s, strike pressure 35 mTorr, O_2 50 sccm, Ar 50 sccm) was carried out to remove the PMMA and graphene in the sample except for under the PS spheres.

The PS spheres and the rest of the PMMA was then removed in hot acetone and rinsed in IPA resulting in a sample of randomly organized

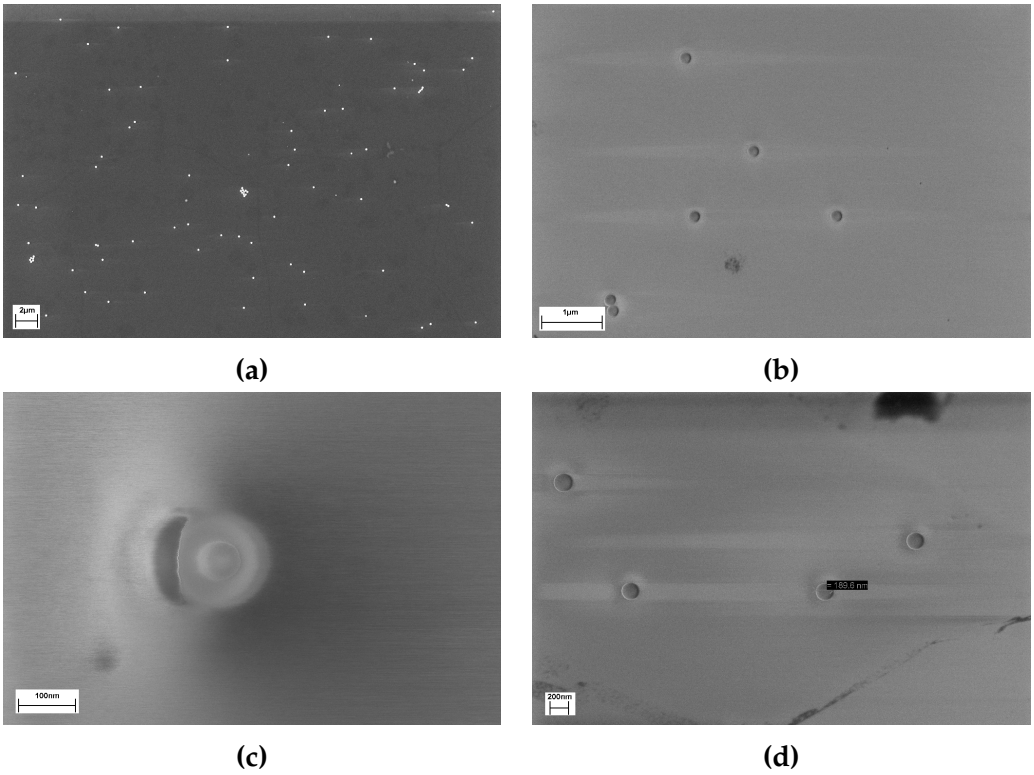

(a) **(b)**

(c) **(d)**

Figure 3.10: SEM images of different stages of manufacturing the graphene nanodisk sample. **a)** Image after deposition of the PS spheres and before the powerful RIE etch. Barely visible are darker spots similar as in figure 3.9a where there are more than one layer of graphene. **b)** Image after etching and before removal with tape. **c)** Image after etching and before removal with tape. Imaging was performed at an angle. Visible is a PS sphere and underneat it the layer of PMMA. **d)** Image after removal with tape.

200 nm graphene nanodisks on a SiO_2/Si substrate. SEM images were not taken from these samples because there is always a risk of damaging the sample by shooting it with electrons. AFM images were taken and some of them can be seen in figures 3.14, 3.15, and 3.16. The graphene nanodisks were around $2.5 - 6$ nm in height so there is probably still some residual PMMA left on top of them or impurities from acetone. The surfaces of the disks were also not smooth but with different kinds of lumps on top of them which is another clear sign of possible impurities.

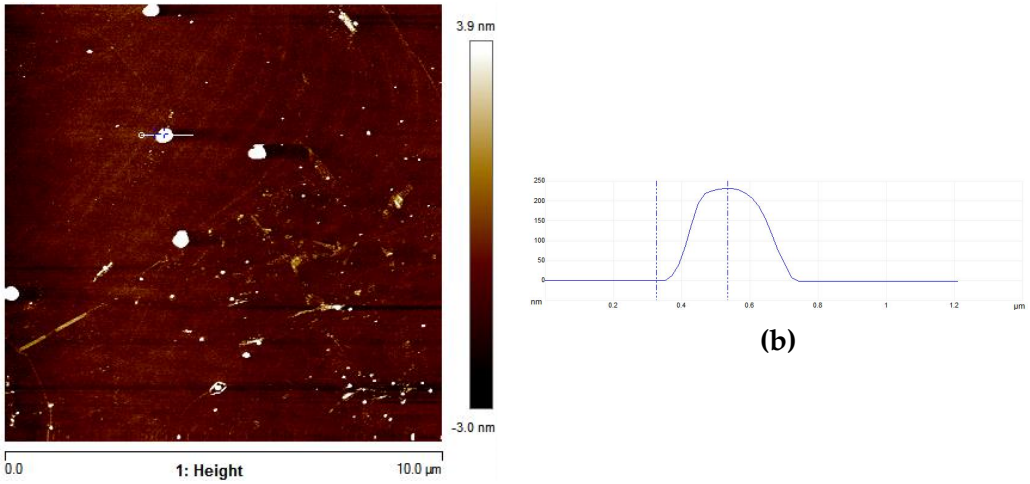

Figure 3.11: a) AFM image of the graphene nanodisk sample after deposition of the PS spheres and the etching. **b)** A height profile of one spot in the same sample along the shown white line.

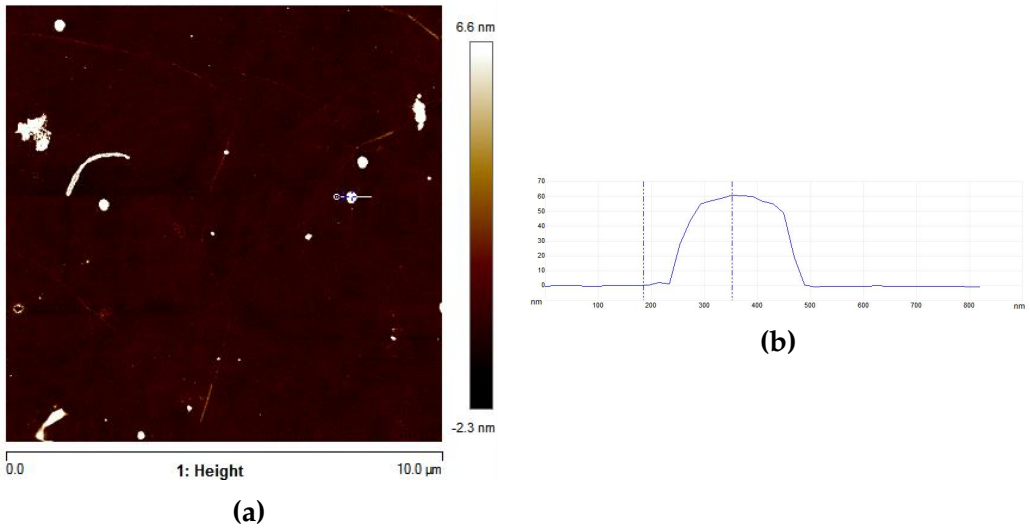

Figure 3.12: a) AFM image of the graphene nanodisk sample after removal of the spheres with tape. **b)** A height profile of one spot in the same sample along the shown white line.

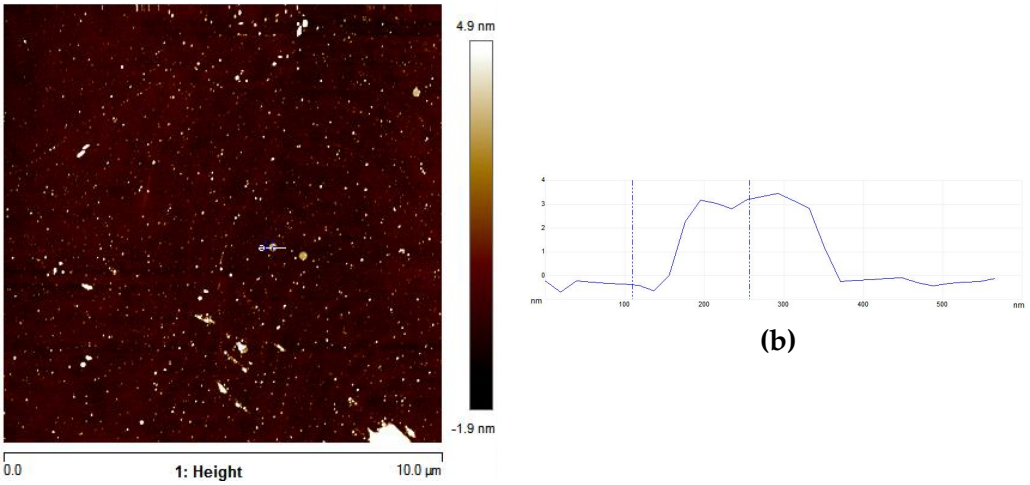

(a) **(b)**

Figure 3.13: **a)** AFM image of the graphene nanodisk sample after removal of the spheres with tape and acetone. **b)** A height profile of one spot in the same sample along the shown white line.

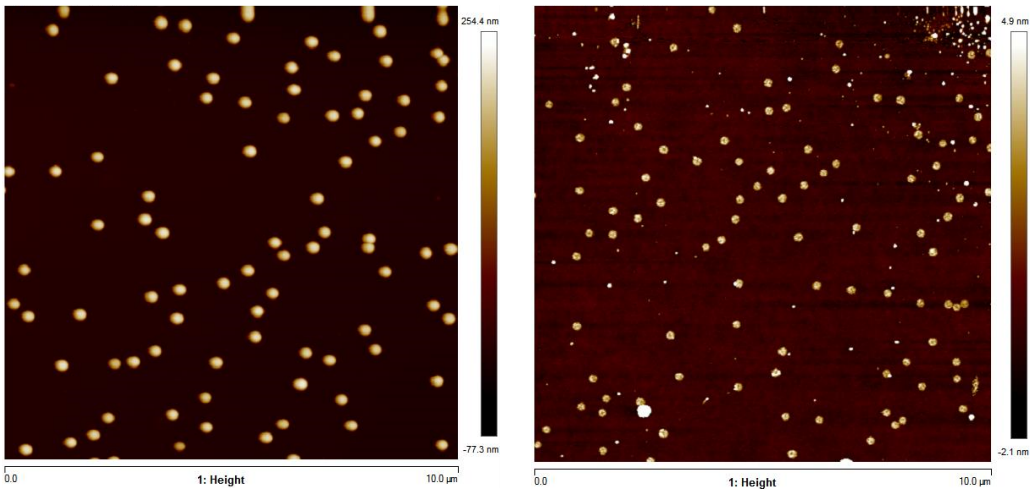

(a) **(b)**

Figure 3.14: AFM images of the graphene nanodisk sample. **a)** Image after deposition of PS spheres but before etching. **b)** Image of the final result after etching and removing spheres and PMMA.

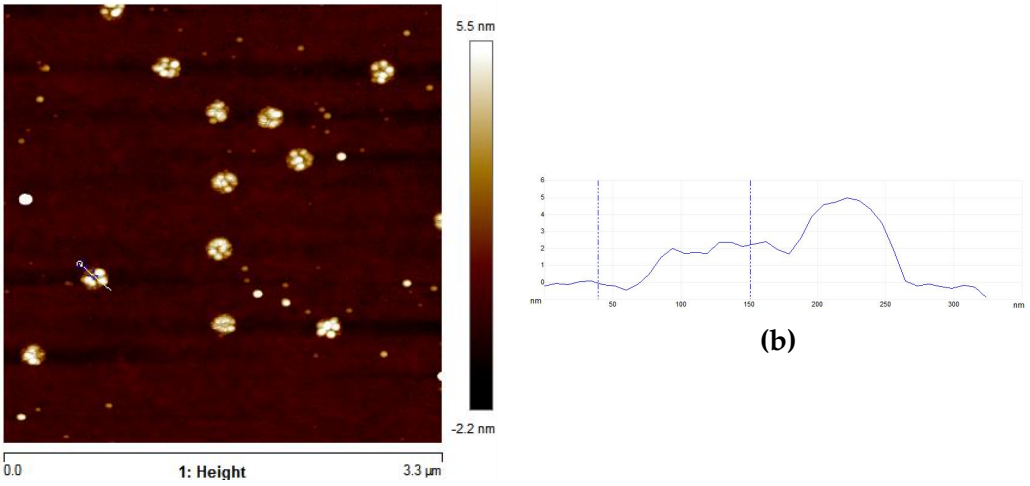

(a) **(b)**

Figure 3.15: a) AFM image of the final result of the graphene nanodisk sample. **b)** A height profile of one spot in the same sample along the shown white line.

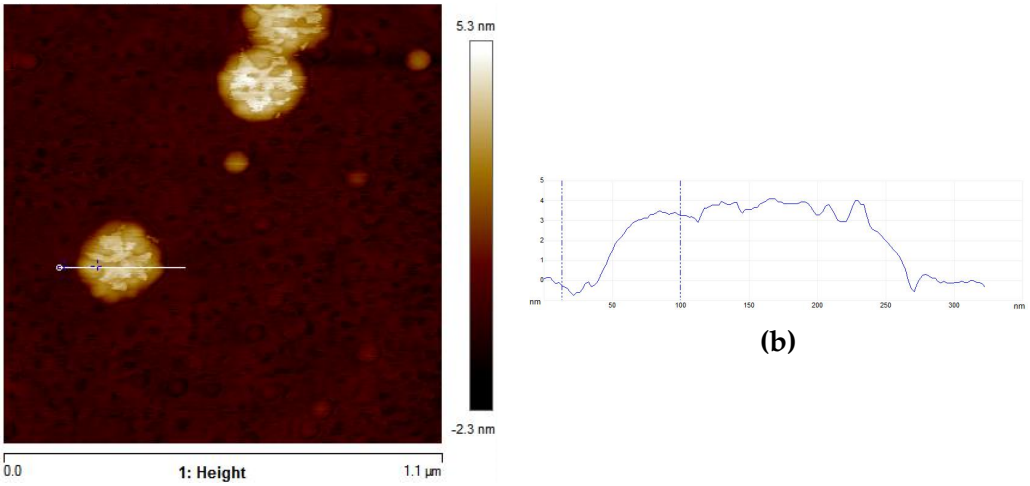

(a) **(b)**

Figure 3.16: a) AFM image of the final result of the graphene nanodisk sample. **b)** A height profile of one spot in the same sample along the shown white line.

3.3 Surface Plasmon Measurements

Fourier-transform infrared (FTIR) spectroscope was used to measure the manufactured samples. In FTIR an infrared spectrum of absorption or emission of a sample is obtained over a wide range of wavelengths simultaneously, which is different if compared to dispersive spectroscopy methods where only a small range of wavelengths can be measured at a time. FTIR also uses Fourier transform processes to convert the collected data into a spectrum.

Some of the untouched graphene samples that were bought from Graphenea were prepared for electrical doping by evaporating 30 nm of Au on the corners of the sample and attaching electrical bonds to them to use those Au patches as electrodes. There were lots of problems with the gating. The graphene was typically in contact with the silicon substrate underneath which is not wanted. The middle part of the sample was tried to be isolated by scratching part of the graphene away to leave a squared graphene area in the middle of the sample so that the gating would not extend to the edges of the sample to make sure there is no contact with the silicon underneath the graphene and SiO_2. This was not very successful either though. The gating problems were most likely due to the poor quality of the bought graphene samples.

Various kinds of FTIR spectroscopes were attempted to be used to measure reflection spectra but in the end a FTIR microscope (Spectra-Tech IR-Plan Advantage) was chosen. A FTIR microscope combines spectroscopic measurements with the ability to visually inspect the samples with a microscope. This microscope was used to measure reflection spectra of these graphene samples from an area of around 10 µm x 10 µm. Firstly to try to see some characteristics to graphene but nothing interesting was visible in the spectra. Then the graphene samples were measured with different applied gate voltages to see similar results as seen in figure 2.7 but nothing was seen again and no good results were obtained.

The manufactured graphene samples were then measured again with the FTIR microscope to see if any plasmon peaks were visible and afterwards the samples were measured with an applied gate voltage but no plasmon peaks were visible in any of the samples and no good results were obtained. The spectra were taken at a range of $650 - 6000\,\mathrm{cm}^{-1}$. According to figure 2.9 plasmon peaks from 200 nm graphene nanodisks should be visible in the very low end of the spectrum, around $650\,\mathrm{cm}^{-1}$ but they

should still be visible in these experiments if they are there and with increased gate voltage peaks should be visible in that range. An example of measured spectra of a graphene nanodisk sample with different gate voltages can be seen in figure 3.17. No plasmons are visible and the miniscule changes seen in the spectra can attributed to possible changes in the measurement system or conditions.

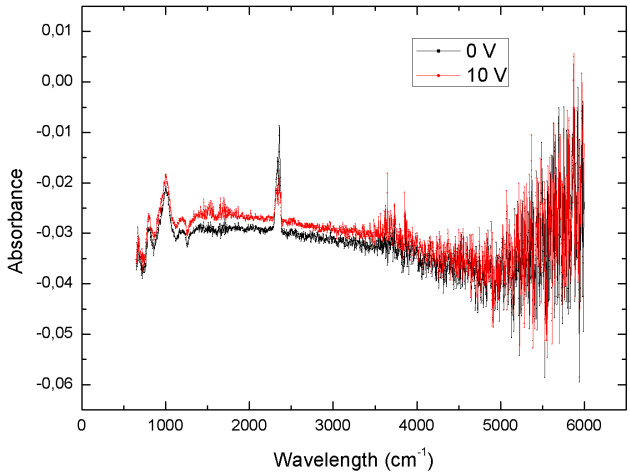

Figure 3.17: Measured spectra of a graphene nanodisk sample with different gate voltages applied. A clean Si/SiO_2 substrate used as a background.

Various methods were attempted to see some sort of peaks in any of the samples. The spectra were usually measured in ambient conditions but at times with N_2 conditions instead of air but no difference. The focus of the spectroscope was attempted to be changed multiple times with miniscule changes but to no avail. Also the position of the sample was moved multiple times to see results from all around the sample. Even though the manufactured graphene samples most likely still contained some traces of PMMA, any peaks of PMMA were not seen either in any of the spectra. In the end no good results were obtained from these spectroscopy measurements and no plasmons were seen.

4 Discussion and Conclusions

The manufacture of the graphene nanodisks samples was all in all rather successful. The steps needed to find the ideal fabrication methods went well although statistically speaking there were not nearly enough of samples made to draw absolutely definite conclusions. During the process of finding the ideal fabrication methods there could have been a lot more of samples made and the parameters could have been studied more thoroughly even though the decisions made seemed quite evident even from the small sample size. But statistical confidence in the methods could be much higher.

The final graphene nanodisk sample discussed in chapter 3.2.7 had an excellent distribution of PS spheres where there is a good amount of them but they are not too much in clusters but rather they are spread out across the sample within good distances. Also good amount of the surface of the sample was covered with the spheres so in that sense the sample was excellent. This also obviously led to the similar distribution of graphene nanodisks in the sample. The height of the graphene nanodisks was around $2.5 - 6\,\text{nm}$ which means that there is still most likely some PMMA residue on top of the nanodisks. The removal with acetone was therefore not quite ideal and it also seemed to leave some impurities in the sample. Unfortunately, that has to be done quite carefully to make sure not to damage any of the graphene nanodisks. More experiments could have been made regarding the final cleaning process to achieve better results with less impurities and perhaps managing to remove the rest of the PMMA residue as well.

The melting of PS spheres on top of the samples was not needed in the end because the etching process seemed anisotropic enough which can be seen from many of the pictures where either the spheres or nanodisks are round and do not have any kind of roughness on the edges which would happen if the etch would be isotropic. The size of the spheres and disks always seemed to be around the correct 200 nm.

There could be many reasons for the different kinds of gating problems encountered with the initial graphene samples. Perhaps the graphene samples were not so good after all to begin with and not uniform enough in graphene. Or perhaps there were some defects in the oxide layer that resulted in the graphene layer being in contact with the silicon substrate

despite the SiO_2 layer between them. It could be also that the evaporated gold electrodes were too far apart from each other and so the graphene in between them could more easily have some defects and the contact could be cut but the gold electrodes were tried to be evaporated more close to each other and that did not solve the problems. Also the bonding process of the electrical bonds into the sample might have been damaging since the graphene samples are quite sensitive. A problem might also be that the graphene might not be grounded in any way so that there is actually no potential differences and changing the gate voltage would be useless. Ion gels could be used like in [24] to achieve better results.

The surface plasmon measurements were obviously a huge failure since no plasmon peaks could be seen in any of the samples. This is quite peculiar because the plasmons should be quite absorptive and should be visible fairly easily if they are present in the samples. There could be numerous possible explanations for this.

Maybe the graphene nanodisk samples were not quite as good as originally thought and as it appeared from pictures. It could be that the etching process removed most of the graphene away leaving just some impurities although I think that is quite unlikely. The initial graphene samples might have not been so great as mentioned earlier so maybe the graphene was not uniform enough to produce any plasmons although the graphene looked to be in good condition when looking at the initial graphene samples with SEM and AFM. The residue PMMA on top of the nanodisks could also possibly be preventing the plasmons peaks from showing up in spectra and either using something else than PMMA such as polyethylene as the mask or performing some more research on removing and cleaning the samples from impurities and extra PMMA during the final fabrication steps could lead to better results. But since even any of the PMMA peaks could not be seen in the spectra then perhaps there is something else wrong.

Perhaps then the problem might lie with the FTIR microscope though the origin of the problem could be difficult to determine. Focusing the microscope was extremely sensitive and even though the focus was always tried to be kept at an ideal level with some miniscule changes attempted, perhaps there were some focusing problems but that seems unlikely. The microscope could also be too sensitive to outside influences, i.e., the background noise could mask all the interesting information or might prevent the interesting peaks from showing up although the background noise

was always removed from the measurements and the air was tested to be removed from the measurements replacing it with just N_2 but that made no difference. Maybe the used FTIR microscope just was not good enough to measure these kinds of extremely thin samples even though FTIR spectroscopes in general have been used to measure graphene samples with great success.

Another possible reason could also be that the coverage of the graphene nanodisks was not high enough, meaning that there were not enough nanodisks in the measured area for the resonances to properly appear in spectra. A more concentrated nanodisk sample could have been tested but that quickly leads to the problem of clusters of nanodisks forming which is not wanted. Considering the other problems encountered, this might not be the real reason for the unsuccessful plasmon measurements either but could be a factor.

Overall the manufacture of the graphene nanodisk samples was quite successful even though improvements and plenty of more experiments could still be made but regardless the work provided valuable experience in various kinds of nanofabrication methods. The surface plasmon measurements were unfortunately not at all successful but still provided interesting experience when trying to figure out the problems.

References

[1] R. W. Wood. On a remarkable case of uneven distribution of light in a diffraction grating spectrum. *Phil. Mag.*, 4:396–402, 1902.

[2] U. Fano. The theory of anomalous diffraction gratings and of quasi-stationary waves on metallic surfaces. *J. Opt. Soc. Am.*, 31:213–222, 1941.

[3] D. Pines. Collective Energy Losses in Solids. *Rev. Mod. Phys.*, 28:184–198, 1956.

[4] R. H. Ritchie. Plasma Losses by Fast Electrons in Thin Films. *Phys. Rev.*, 106:874–881, 1957.

[5] R. H. Ritchie, E. T. Arakawa, J. J. Cowan, and R. N. Hamm. Surface-Plasmon Resonance Effect in Grating Diffraction. *Phys. Rev. Lett.*, 21:1530–1533, 1968.

[6] A. Otto. Excitation of nonradiative surface plasma waves in silver by the method of frustrated total reflection. *Z. Phys.*, 216:398–410, 1968.

[7] E. Kretschmann and H. Raether. Radiative Decay of Non Radiative Surface Plasmons Excited by Light. *Z. Naturf.*, 23:2135–2136, 1968.

[8] E. Kretschmann. Die Bestimmung optischer Konstanten von Metallen durch Anregung von Oberflächenplasmaschwingungen. *Z. Phys.*, 241:313–324, 1971.

[9] B. Hecht, H. Bielefeldt, L. Novotny, Y. Inouye, and D. W. Pohl. Local Excitation, Scattering, and Interference of Surface Plasmons. *Phys. Rev. Lett.*, 77:1889–1892, 1996.

[10] J. Pendry. Playing Tricks with Light. *Nature*, 285:1687–1688, 1999.

[11] M. Mansuripur, A. R. Zakharian, A. Lesuffleur, S-H. Oh, R. J. Jones, N. C. Lindquist, H. Im, A. Kobyakov, and J.V. Moloney. Plasmonic nano-structures for optical data storage. *Opt. Express*, 17:14001–14014, 2009.

[12] M. Westphalen, U. Kreibig, J. Rostalski, H. Luth, and D. Meissner. Metal cluster enhanced organic solar cells. *Sol. Energy Mat. Sol. Cells*, 61:97–105, 2000.

[13] J. Homola, S. S. Yee, and G. Gauglitz. Surface plasmon resonance sensors: review. *Sensors Actuat.*, 54:3–15, 1999.

[14] B. C. Brodie. On the Atomic Weight of Graphite. *Phil. Trans. R. Soc. Lond.*, 149:249–259, 1859.

[15] G. Rüss and F. Vogt. Höchstlamellarer Kohlenstoff aus Graphitoxyhydroxyd. *Monatshefte Chem.*, 78:222–242, 1948.

[16] H. P. Boehm, A. Clauss, G. O. Fischer, and U. Hofmann. Das Adsorptionsverhalten sehr dünner Kohlenstoff-Folien. *Z. Anorg. Allg. Chem.*, 316:119–127, 1962.

[17] P. Wallace. The Band Theory of Graphite. *Phys. Rev.*, 71:622–634, 1947.

[18] K. S. Novoselov, A. K. Geim, S. V. Morozov, D. Jiang, Y. Zhang, S. V. Dubonos, I. V. Grigorieva, and A. A. Firsov. Electric Field Effect in Atomically Thin Carbon Films. *Science*, 306:666–669, 2004.

[19] K. S. Kim, Y. Zhao, H. Jang, S. Y. Lee, J. M. Kim, K. S. Kim, J-H. Ahn, P. Kim, J-Y. Choi, and B. H. Hong. Large-scale pattern growth of graphene films for stretchable transparent electrodes. *Nature*, 457:706–710, 2009.

[20] J. Wu, H. A. Becerril, Z. Bao, Z. Liu, Y. Chen, and P. Peumans. Organic solar cells with solution-processed graphene transparent electrodes. *Appl. Phys. Lett.*, 92:263302, 2008.

[21] X. Wang, L. Zhi, and K. Mullen. Transparent, Conductive Graphene Electrodes for Dye-Sensitized Solar Cells. *Nano Lett.*, 8:323–327, 2008.

[22] S. Bae et al. Roll-to-roll production of 30-inch graphene films for transparent electrodes. *Nature Nanotechnol.*, 5:574–578, 2010.

[23] T. J. Echtermeyer, L. Britnell, P. K. Jasnos, A. Lombardo, R. V. Gorbachev, A. N. Grigorenko, A. K. Geim, A. C. Ferrari, and K. S. Novoselov. Strong plasmonic enhancement of photovoltage in graphene. *Nature Commun.*, 2:458, 2011.

[24] Z. Fang, S. Thongrattanasiri, A. Schlather, Z. Liu, L. Ma, Y. Wang, P. M. Ajayan, P. Nordlander, N. J. Halas, and F. J. Garcia de Abajo. Gated Tunability and Hybridization of Localized Plasmons in Nanostructured Graphene. *ACS Nano*, 7:2388–2395, 2013.

[25] H. Fredriksson, Y. Alaverdyan, A. Dmitriev, C. Langhammer, D. S. Sutherland, M. Zäch, and B. Kasemo. Hole-Mask Colloidal Lithography. *Adv. Mater.*, 19:4297–4302, 2007.

[26] W. L. Barnes. Surface plasmon-polariton length scales: a route to sub-wavelength optics. *J. Opt. A: Pure Appl. Opt.*, 8:S87–S93, 2006.

[27] M. Dragoman and D. Dragoman. Plasmonics: Applications to nanoscale terahertz and optical devices. *Prog. Quant. Electron.*, 32:1–41, 2008.

[28] A. V. Zayats, I. I. Smolyaninov, and A. A. Maradudin. Nano-optics of surface plasmon polaritons. *Phys. Rep.*, 408:131–314, 2005.

[29] L. Novotny and B. Hecht. *Principles of Nano-Optics*. Cambridge University Press, 2006.

[30] P. Berini, R. Charbonneau, N. Lahoud, and G. Mattiussi. Characterization of long-range surface-plasmon-polariton waveguides. *J. Appl. Phys.*, 98:043109, 2005.

[31] H. Raether. Surface Plasmons on Smooth and Rough Surfaces and on Gratings. *Springer Tr. in Mod. Phys.*, 111, 1988.

[32] A. H. Castro Neto, F. Guinea, N. M. R. Peres, K. S. Novoselov, and A. K. Geim. The electronic properties of graphene. *Rev. of Mod. Phys.*, 81:109–162, 2009.

[33] D. D. L. Chung. Graphite. *J. Mater. Sci.*, 37:1475–1489, 2002.

[34] B. Partoens and F. M. Peeters. From graphene to graphite: Electronic structure around the K point. *Phys. Rev. B*, 74:075404, 2006.

[35] C. Lee, X. Wei, J. W. Kysar, and J. Hone. Measurement of the Elastic Properties and Intrinsic Strength of Monolayer Graphene. *Science*, 321:385–388, 2008.

[36] E. Pop, V. Varshney, and A. K. Roy. Thermal properties of graphene: Fundamentals and applications. *MRS Bull.*, 37:1273–1281, 2012.

[37] K. S. Novoselov, D. Jiang, F. Schedin, T. J. Booth, V. V. Khotkevich, S. V. Morozov, and A. K. Geim. Two-dimensional atomic crystals. *Proc. Natl Acad. Sci. USA*, 102:10451–10453, 2005.

[38] M. Wilson. Electrons in atomically thin carbon sheets behave like massless particles. *Phys. Today*, 59:21–23, 2006.

[39] K. I. Bolotin, K. J. Sikes, Z. Jiang, M. Klima, G. Fudenberg, J. Hone, P. Kim, and H. L. Stormer. Ultrahigh electron mobility in suspended graphene. *Solid State Commun.*, 146:351–355, 2008.

[40] A. K. Geim and K. S. Novoselov. The rise of graphene. *Nat. Mater.*, 6:183–191, 2007.

[41] K. S. Novoselov, Z. Jiang, Y. Zhang, S. V. Morozov, H. L. Stormer, U. Zeitler, J. C. Maan, G. S. Boebinger, P. Kim, and A. K. Geim. Room-Temperature Quantum Hall Effect in Graphene. *Science*, 315:1379, 2007.

[42] R. R. Nair, P. Blake, A. N. Grigorenko, K. S. Novoselov, T. J. Booth, T. Stauber, N. M. R. Peres, and A. K. Geim. Fine Structure Constant Defines Visual Transparency of Graphene. *Science*, 320:1308, 2008.

[43] A. B. Kuzmenko, E. van Heumen, F. Carbone, and D. van der Marel. Universal Optical Conductance of Graphite. *Phys. Rev. Lett.*, 100:117401, 2008.

[44] P. Avouris and M. Freitag. Graphene Photonics, Plasmonics, and Optoelectronics. *IEE J. Sel. Topics Quantum Electron.*, 20:72–83, 2014.

[45] S-E. Zhu, S. Yuan, and G. C. A. M. Janssen. Optical transmittance of multilayer graphene. *Europhys. Lett.*, 108:17007, 2014.

[46] F. Wang, Y. Zhang, C. Tian, C. Girit, A. Zettl, M. Crommie, and Y. R. Shen. Gate-Variable Optical Transitions in Graphene. *Science*, 320:206–209, 2008.

[47] X. Luo, T. Qiu, W. Lu, and Z. Ni. Plasmons in graphene: Recent progress and applications. *Mater. Sci. Eng. R-Rep.*, 74:351–376, 2013.

[48] G. W. Hanson. Dyadic Green's Functions and Guided Surface Waves for a Surface Conductivity Model of Graphene. *J. Appl. Phys.*, 103:064302, 2008.

[49] M. Jablan, H. Buljan, and M. Soljačić. Plasmonics in graphene at infrared frequencies. *Phys. Rev. B*, 80:245435, 2009.

[50] F. H. L. Koppens, D. E. Chang, and F. J. García de Abajo. Graphene Plasmonics: A Platform for Strong Light-Matter Interactions. *Nano Lett.*, 11:3370–3377, 2011.

[51] P. Tassin, T. Koschny, M. Kafesaki, and C. M. Soukoulis. A comparison of graphene, superconductors and metals as conductors for metamaterials and plasmonics. *Nat. Photon.*, 6:259–264, 2012.

[52] W. B. Lu, W. Zhu, H. J. Xu, Z. H. Ni, Z. G. Dong, and T. J. Cui. Flexible transformation plasmonics using graphene. *Opt. Express*, 21:10475–10482, 2013.

[53] L. Ju, B. Geng, J. Horng, C. Girit, M. Martin, Z. Hao, H. A. Bechtel, X. Liang, A. Zettl, Y. R. Shen, and F. Wang. Graphene plasmonics for tunable terahertz metamaterials. *Nat. Nanotechnol.*, 6:630–634, 2011.

[54] H. Yan, F. Xia, Z. Li, and P. Avouris. Plasmonics of coupled graphene micro-structures. *New J. Phys.*, 14:125001, 2012.

[55] P. Liu, W. Cai, L. Wang, X. Zhang, and J. Xu. Tunable terahertz optical antennas based on graphene ring structures. *Appl. Phys. Lett.*, 100:153111, 2012.

[56] H. Yan, X. Li B. Chandra, G. Tulevski, Y. Wu, M. Freitag, W. Zhu, P. Avouris, and F. Xia. Tunable infrared plasmonic devices using graphene/insulator stacks. *Nat. Nanotechnol.*, 7:330–334, 2012.

[57] S. Franssila. *Introduction to Microfabrication*. Wiley, 2004.

[58] J. Goldstein, D. E. Newbury, D. C. Joy, C. E. Lyman, P. Echlin, E. Lifshin, L. Sawyer, and J. R. Michael. *Scanning Electron Microscopy and X-ray Microanalysis*. Springer, 3rd edition, 2003.

[59] JEOL LTD. Invitation to the SEM World.

[60] F. J. Giessibl. Advances in atomic force microscopy. *Rev. Mod. Phys.*, 75:949, 2003.